Dynamic Soaring for Fixed-Wing UAVs

by

Bernhard Paus Græsdal

Submitted to the Department of Engineering Cybernetics
in partial fulfillment of the requirements for the degree of

Master of Science

at the

Norwegian University of Science and Technology

December 2020

Author .....
Department of Engineering Cybernetics
December 17th, 2020

Certified by .....
Morten Dinhoff Pedersen
Associate Professor
Thesis Supervisor

Dynamic Soaring for Fixed-Wing UAVs

by

Bernhard Paus Græsdal

Submitted to the Department of Engineering Cybernetics
on December 17th, 2020, in partial fulfillment of the
requirements for the degree of
Master of Science

Abstract

Dynamic Soaring is a technique where birds exploit wind fields to maintain energy-neutral flight over very long distances, without flapping their wings. This work examines the application of dynamic soaring to unmanned aerial vehicles (UAVs).

First, a novel analysis of the energy mechanisms during soaring flight is presented, and it is shown how this analysis generalizes to all models typically used for dynamic soaring. Then, a new 3-DOF point-mass model of a glider flying through a wind shear is derived. This model emphasizes understanding of the motion of a glider, as well as simplicity in terms of physical glider parameters. Next, a trajectory optimization approach known as Direct Collocation will be utilized to generate soaring trajectories. The method is explained in detail, and the problem of dynamic soaring is formulated as an optimal control problem.

Finally, numerical results are generated for dynamic soaring trajectories in all angles to the wind. The numerical results are analyzed, and the energy analysis from the beginning of the thesis is verified. The dynamic soaring trajectories are shown to be similar to those observed in nature. Future directions for work on dynamic soaring are proposed.

Thesis Supervisor: Morten Dinhoff Pedersen
Title: Associate Professor

Contents

Chapter 1

Introduction to Dynamic Soaring

In nature, birds are often seen gliding with the wind. By exploiting wind gradients during their flight, birds are able to cover great distances with very little flapping of their wings. In some cases, bird species have been able to travel distances far longer than what their body mass and energy expenditure would indicate as possible. The most extreme case is perhaps found for the Wandering Albatross. By using a very special flight technique, it has been documented circumnavigating the globe in as little as 46 days [1]. This special flight technique is called *dynamic soaring*, and is the topic of this thesis.

Figure 1-1: The Wandering Albatross.

The phenomenon of dynamic soaring has received attention since 1883, when Lord Rayleigh first attempted to analyse the flight of the albatross [2]. Today, it is still an ongoing topic of research, and the world has yet to see a real-life UAV capable of

exploiting the potential of dynamic soaring. The aim of this thesis is to contribute to the field of dynamic soaring, by exploring the trajectories required for dynamic soaring flight.

To give the reader a taste of the concept, a glider performing dynamic soaring to travel in an energy-neutral manner at a direction normal to the wind can be seen in fig. 1-2. Through periodic motion, the glider extracts energy from the wind. In theory, this allows the glider to sustain infinite flight without the need for a thrust-generating propeller or big energy reserves. Later in the thesis, the inner workings of how such a trajectory works to harvest energy, and how it can be generated, will be explored.

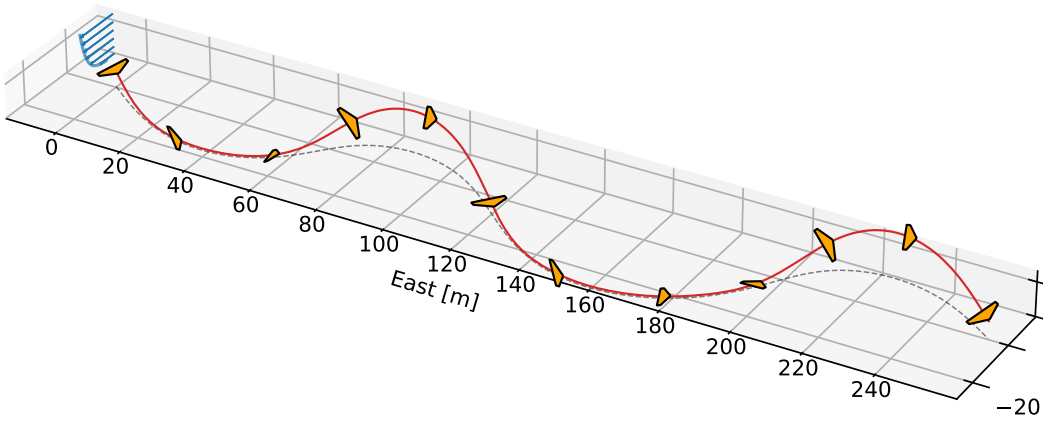

Figure 1-2: Example of dynamic soaring

1.1 Basic Concepts of Soaring Flight

There are multiple different types of soaring flight, of which dynamic soaring is a specific type. Before diving into the concept of dynamic soaring, soaring flight in general should be categorized. It is common to divide soaring flight into different categories [3, 4], and generally, one can make a distinction between

- Gust soaring

- Thermal soaring
- Slope soaring
- Dynamic soaring

Gust soaring is defined as the process of extracting energy from high frequency turbulence in the atmosphere [5], and is its own field of research. Thermal soaring is the use of warm updraughts causing vertical wind components, while slope soaring is the use of vertical winds caused by terrain qualities such as hills and mountains. Both thermal and slope soaring are types of soaring that can be categorized as *static* soaring, as the majority of energy gained with these methods is obtained through a steady vertical component of the wind. The two types of static soaring are techniques that have been utilized by sailplane pilots and RC hobbyists for a long time. As an example, in 2018 the worlds record for the fastest RC airplane was achieved at a stunning 877kmh^{-1} using slope soaring [6]. Although interesting, neither gust soaring, slope soaring or thermal soaring will be the focus of this thesis.

Finally, we are left with *dynamic* soaring. Dynamic soaring can be described as the process of extracting energy from a wind field by flying specific, periodic maneuvers through the wind. It is this type of soaring that is utilized by birds to travel very long distances with very little energy expenditure, and because of its huge potential, it has been an active area of research for a long time. Despite the attention devoted to the problem over the years, the world has yet to see a real-life robotic albatross flying across the Atlantic by utilizing only wind gradients as its main energy source.

1.2 Relevant Work

As the topic of dynamic soaring has received quite a bit of attention over the years, many aspects have already been explored. Generation of dynamic soaring trajectories has been achieved with different methods, and researchers report to be able to do this at real-time rates [4, 7, 8, 9]. Typically, optimal control techniques have given good results [3, 4, 7, 8, 9, 10, 11, 12, 13, 14, 15, 16]. Other methods such as genetic

algorithms [17], reinforcement learning [18] and even explicit integration of closed-form dynamics [19] have also been used. Online estimation of the wind field during flight has received attention by multiple researchers [9, 13, 20], and the effect of varying the wind shear is also very explored [4, 7, 10, 11]. Online stabilization of the generated trajectories has been tested by different methods in simulation [9, 20, 21]. Many of these works include an energy analysis, which commonly depends upon specific details of the model or implementation, such as glider attitude or wind modelling. In this subsection, a brief overview of some of the most influential work will be covered.

Zhao et al. are amongst the first to present a promising method for real-time implementation of dynamic soaring in their work [7, 8]. Here, they present the dynamics of a fixed-wing glider as a point-mass model, while generating dynamic soaring trajectories with trajectory optimization. The trajectory optimization problem is converted into a parameter optimization problem and solved numerically with a collocation method together with a general, non-linear solver. A number of different optimization objectives are investigated, namely the minimization of the cycle times, maximization of altitude gain after a cycle, and the minimum required wind shear gradients to sustain energy-neutral trajectories. The point-mass model used by Zhao in this work is used in many of the following works.

Similar to the model used by Zhao, Sachs presents a new dynamical model in [3]. It was shown by [4] that these two models are in fact equal. The input is chosen as the bank angle and the lift coefficient of the glider. Using this model, Sachs generates dynamic soaring trajectory for both the case where the lift coefficient is allowed to vary freely, and for the case where it is constrained to be a constant value. The trajectory optimization implementation is not detailed, but Sachs likely used the same shooting approach found in his other work [22]. Later, in [14], real albatrosses are tracked by GPS, and the flight path is analyzed. An energy analysis of the flight of the albatross is also performed.

In [12], Deittert et al. further explore the dynamics from [7], by showing how these dynamics are differentially flat. By using the differential flatness property, the

trajectory can be generated in a lower-dimensional space, reducing the complexity of the problem. In their work, periodic trajectories are generated using Fourier series for describing the flat outputs, while adding constraints through the differential flatness property of the system. In addition to this, the likelihood of favorable winds is predicted based on weather statistics, and it is shown that the ability to fly close to the surface is a key factor in dynamic soaring performance.

A survey of how dynamic soaring trajectories are normally generated, as well as the models that are typically used, is given in [13]. The survey gives a brief overview over the different trajectory optimization techniques that have historically been used, including different objectives for the optimization problem and different optimal control formulations.

In his dissertation [4], Bower performs an very in-depth analysis of dynamic soaring planning and aircraft design for small UAVs. The 3-DOF models used by Zhao [7] and Sachs [3] are compared, and different wind models are considered. Management of onboard electrical energy to power sensors, communications, and actuators are analyzed, and dynamics for the state of onboard electrical energy is derived. In the case of a solar powered vehicle, an energy analysis is also performed. Further, multiple different trajectory optimization techniques are tested and compared for the purpose of dynamic soaring, and Direct Collocation is chosen as the most efficient and robust technique. Ocean wave analysis close to the surface is performed, and is incorporated into the trajectory optimization. Analysis is performed on the generated trajectories to get information about the minimum wind speed and the maximum achievable airspeed of the glider. Design guidelines for a UAV specifically built for dynamic soaring is proposed, based on the analysis. Further, a high-level planning algorithm based on isochrones is implemented for higher order planning across multiple different wind fields.

A full 6-DOF model of an airplane is utilized to generate trajectories in [15]. This is in contrast to a lot of existing work, as very little work focuses on generating trajectories for the full 6-DOF state space of a glider. In this work, the model is shown to be differentially flat, similar to the work in Deittert in [12], which is used to

reduce the problem complexity. The dynamics are shown to be differentially flat in the output space of the aircraft's position and attitude time-history, and the authors claim that this reduction in dimensionality is sufficient to generate real-time trajectories. However, the work shows that the 6-DOF trajectory optimization problem is very sensitive to the initial guess, and a 3-DOF trajectory optimization problem is actually solved first in order to obtain good initial guesses. The authors propose to use this method for real-time implementation, where the higher order solutions are computed successively by using the low order solutions as initial guesses.

Recently, the investigation of the effects of different wind shears is examined by Slotine et al. in [10, 11]. Here, the same low-order model as used by Zhao in [7] is used to in combination with a logistic wind shear model to explore the minimum-wind trajectories for different shear layer thicknesses. Trajectories for both loitering and travelling maneuvers are found, and the trajectory optimization is solved by using Direct Collocation. The behaviour around a very thin wind shear with a thickness that approaches zero is explored, as well as how behaviour is affected by large glide ratios. From these simplifications, low-order analytical expressions are derived, from which qualitative conclusions on topics like airspeed change and the importance of wind separation after waves are drawn.

A recent technique that exploits dynamic soaring to optimize fuel use of a fixed-wing UAV is presented by Akhtar et al. in [9]. The goal is not to perform pure dynamic soaring, but to increase the range of an UAV, by combining the use of a propeller with optimal soaring trajectories. Here, the differentially flat dynamics presented by [7, 12] are used. This is combined with a trajectory optimization method first proposed by Yakimenko in [23], in order to generate real-time trajectories. The method is known as *the Inverse Dynamics in the Virtual Domain (IDVD)*, and parametrizes the trajectory in terms of high-order, global, polynomials, where the coefficients are determined by the initial and final values of the derivatives of the trajectory. Akhtar et al. report to generate trajectories within the order of 10 seconds, which, given trajectories of lengths between 20 to 1000 seconds, allows for computation of the next trajectory before the previous trajectory is fully executed.

They further propose a method for online wind estimation using the standard least squares method, which allows the next trajectory to be computed based on the updated wind model. The results are verified in simulation on a full 6-DOF glider model, where the trajectories are followed using a PID-controller.

Focusing on the online stabilization and correction of trajectories during flight, Hong et al. presents a promising real-time quadratic programming approach in their recent work [21]. Here, a periodic, energy-neutral dynamic soaring trajectory is the starting point, and by using instant wind information, the trajectory is corrected during flight. By formulating a strictly convex quadratic programming problem based on the sensitivity relation between the increment of the wind strength, the predicted error and the input corrections, control inputs can be corrected in real-time. By using this method, the complete wind shear does not need to be known in advance, and the strength of the method is demonstrated in simulation. For their work, the model presented in [3, 22] is used.

In another recent work by Kai et al. [19], a new way of modelling the aerodynamic forces acting on a glider is presented, in combination with generation of dynamic soaring trajectories. By using this model, a new perspective is given on the energy extraction process during dynamic soaring flight. A way of expressing a glider performing dynamic soaring along a trajectory as a closed-form finite-dimensional ODE is proposed, which can then be solved using standard integration schemes to obtain a soaring trajectory that will keep the glider aloft. However, the found trajectory is not necessarily optimal in any sense, which is where this paper departs from other similar work.

An interesting perspective is taken by the researchers in [20], where their work is focused on bringing autonomous dynamic soaring closer to a reality. In their own words, the authors propose methods for "closing the loop in dynamic soaring", by implementing online wind estimation for complex wind fields, trajectory planning, and path-following control in a single system. The performance of the system is assessed through Monte Carlo simulations, and a hardware-in-the-loop simulation is performed with a commercial flight controller. For strong shear layers, the authors conclude that

autonomous dynamic soaring is viable using currently available hardware, trajectory planners and control policies.

1.3 Thesis Contributions

The work in this thesis has been focused around a novel analysis of the energy mechanisms in dynamic soaring, in combination with the derivation of a new model of a glider flying through a wind field. Motivated by the fact previous energy analysis of soaring flight tends to rely on modelling detail, the presented analysis will be completely void of such details, while retaining a precise conclusion. In this work the following contributions are made to the topic of dynamic soaring:

- A more general analysis of how a glider flying through a wind field harvests energy is proposed. The analysis generalizes to a broad number of models and cases. To the author's knowledge, this is the most general energy analysis yet proposed within the field of dynamic soaring.

- It is shown how the energy analysis applies to a broad class of wind fields, including all the wind models typically used in the context of dynamic soaring.

- A novel 3-DOF point-mass model of a glider flying through a general wind field is introduced, aiming to make the motion of a glider through a wind field more intuitive.

- It is shown how the characteristic motion of a glider through a wind field only depends on a single physical parameter of the glider. This is shown by reformulating and rescaling the model in terms of the optimal lift-to-drag ratio.

- Both the energy analysis and the new model are verified and tested by generating dynamic soaring trajectories through a standard trajectory optimization technique called Direct Collocation.

1.4 Thesis Outline

In chapter 2, a novel analysis of the energy mechanism that enables dynamic soaring will be explained in detail. In chapter 3, a new model for a glider flying through a wind field will be presented, in the spirit of the energy analysis. In chapter 4, the problem of generating dynamic soaring trajectories will be formulated as an optimal control problem, and the trajectory optimization technique known as Direct Collocation will be detailed. In chapter 5 the generated trajectories will be presented and analysed. Finally, in chapter 6, directions for future work will be proposed, and final conclusions based on this work will be drawn.

Chapter 2

Harvesting Energy through Periodic Motion

The goal of dynamic soaring is to harvest energy from a wind field in order to sustain energy-neutral (or even energy-positive) flight, and this is achieved through periodic motion. Many researchers have proposed different analyses of the energy extraction process that takes place during soaring flight [3, 4, 7, 8, 9, 10, 11, 12, 13, 14, 15, 19]. All of these analyses have in common that they rely on details regarding either modelling of aerodynamic forces, glider dynamics or wind modelling to explain the energy mechanisms during dynamic soaring.

Here, a novel approach for analyzing energy gain through dynamic soaring is proposed, based only on Newtons Second Law of Motion. The analysis explains how it is possible to gain energy through the use of periodic motion, without going into the aforementioned details. The energy analysis will be shown to generalize to all 3-DOF point-mass models used to describe gliders, and to a broad class of wind models, including those typically used in the context of dynamic soaring. Despite its simplicity, the analysis retains a very precise conclusion.

2.1 Background

In general, wind gradients in the atmosphere is what makes dynamic soaring possible. Wind speeds tends to increase with height, and birds exploit this property to extract energy from the wind. Due to friction from the ground, the wind speed is slowed significantly closer to the ground, a condition that is normally referred to as the no-slip condition [24]. Because of this, the wind speed normally increases quickly with altitude, giving rise to significant wind gradients. By performing aerodynamic maneuvers in the vicinity of these wind gradients, birds are able to gain energy, sustaining energy-neutral flight.

Simple analysis on infinitesimally small wind shears, where the wind is zero below a certain point and constant above it, reveals that in order to extract energy, the bird has to travel with the wind where the wind is strongest, and against the wind where the wind is weakest. This was first explored by Lord Rayleigh himself in [2]. This is a simplification, as the analysis gets more complicated for flight in more complex wind fields. Simple analysis also shows some trivial results, for example that the drag always reduces the energy in the system, and that a wind with an updraft component will increase the energy of the system. However, these results do not explain how energy is gained through dynamic soaring maneuvers.

A key aspect in all dynamic soaring trajectories is that it is not possible to extract energy from the wind at all points along the trajectory. In other words, it is unavoidable that energy will be lost at some points. Therefore, a trajectory is designed to achieve greater *total* energy gain compared to the total energy loss. This aspect of trading energy now for the potential of gaining energy later is vital in the trajectory design for soaring trajectories.

2.2 Energy Analysis

The derivation in this chapter builds upon and follows closely the work of this thesis' supervisor, Morten D. Pedersen, in [25].

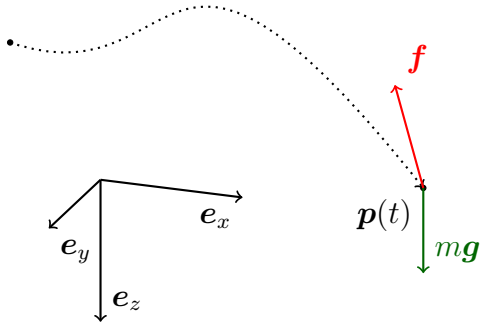

Figure 2-1: A point mass under the influence of gravitational and aerodynamic forces in the NED coordinate frame.

The simplest description of a glider flying through a wind shear is found from Newton's Second Law of Motion, describing the dynamics of a point-mass under the influence of an aerodynamic force $\boldsymbol{f}$ and the gravitational force $m\boldsymbol{g} = mg\boldsymbol{e}_z$:

$$m\dot{\boldsymbol{v}} = \boldsymbol{f} + mg\boldsymbol{e}_z \tag{2.1}$$

$$\dot{\boldsymbol{p}} = \boldsymbol{v} \tag{2.2}$$

where $\boldsymbol{p} = \boldsymbol{p}(t)$ denotes the position of the point-mass, and $\boldsymbol{v} = \boldsymbol{v}(t)$ denotes the velocity. An illustration of this can be found in fig. 2-1. Further, let the relative velocity, or the airspeed, of the glider, be denoted as

$$\boldsymbol{v}_a = \boldsymbol{v} - \boldsymbol{w} \tag{2.3}$$

where $\boldsymbol{w} = \boldsymbol{w}(\boldsymbol{p}, t)$ denotes the wind velocity. Let the aerodynamic force consist of two perpendicular forces

$$\boldsymbol{f} = \boldsymbol{l} + \boldsymbol{d} \tag{2.4}$$

namely the lift $\boldsymbol{l} \perp \boldsymbol{v}_a$ and the drag $\boldsymbol{d} \parallel \boldsymbol{v}_a$. Because the drag is always acting in the opposite direction of the relative velocity, we also have that $\boldsymbol{d}^\intercal \boldsymbol{v}_a < 0$.

For our energy analysis, we start by looking at the kinetic and potential energy

of the system:

$$E_{kin} = \frac{1}{2} m |\boldsymbol{v}|^2 \tag{2.5a}$$

$$E_{pot} = mgh \tag{2.5b}$$

where the time derivatives of E_{kin} and E_{pot} are given as

Fix NED frame etc here

$$\frac{d}{dt}\left(\frac{1}{2} m |\boldsymbol{v}|^2\right) = m\boldsymbol{v}^\intercal \dot{\boldsymbol{v}} = m\boldsymbol{v}_a^\intercal \dot{\boldsymbol{v}} + m\boldsymbol{w}^\intercal \dot{\boldsymbol{v}} \tag{2.6a}$$

$$\frac{d}{dt}(mgz) = mg\dot{z} \tag{2.6b}$$

Next, the point mass dynamics in eq. (2.2) is dotted with the relative velocity to obtain:

$$\begin{aligned} m\boldsymbol{v}_a^\intercal \dot{\boldsymbol{v}} &= \boldsymbol{v}_a^\intercal \boldsymbol{f} + mg\boldsymbol{v}_a^\intercal \boldsymbol{e}_z = \boldsymbol{v}_a^\intercal \boldsymbol{f} + mg\boldsymbol{v}^\intercal \boldsymbol{e}_z - mg\boldsymbol{w}^\intercal \boldsymbol{e}_z \\ &= \boldsymbol{v}_a^\intercal \boldsymbol{f} - mg\dot{h} - mgw_z \\ &= \frac{d}{dt}\left(\frac{1}{2} m |\boldsymbol{v}|^2\right) - m\boldsymbol{w}^\intercal \dot{\boldsymbol{v}} \end{aligned} \tag{2.7}$$

where $h \triangleq -z$ is defined as the height of the glider. The relation in eq. (2.6a) is used to arrive at the result in the last line. Rearranging gives an expression for the power of the entire system

$$\dot{E} = \frac{d}{dt}\left(\frac{1}{2} m |\boldsymbol{v}|^2 + mgh\right) = \boldsymbol{v}_a^\intercal \boldsymbol{f} + m\dot{\boldsymbol{v}}^\intercal \boldsymbol{w} - mgw_z \tag{2.8}$$

This equation describes how energy enters the system and how energy is lost, and will be the basis for the energy analysis.

We start by investigating whether energy-neutral flight can be achieved. By looking at the first term in eq. (2.8), we can define the power dissipation due to drag as

$$\mathcal{D} \triangleq -\boldsymbol{v}_a^\intercal \boldsymbol{f} = -\boldsymbol{v}_a^\intercal \boldsymbol{d} > 0 \tag{2.9}$$

Next, define the soaring power in the system as

$$\mathcal{S} \triangleq m\dot{\boldsymbol{v}}^\intercal \boldsymbol{w} - mgw_z \tag{2.10}$$

This allows for the following, compact reformulation of the overall power of the system:

$$\dot{E} + \mathcal{D} = \mathcal{S} \tag{2.11}$$

From this, it is clear that if $\mathcal{S} \geq \mathcal{D} > 0$ on average over a trajectory, the overall energy in the system will be increased, or at the very least maintained at a constant level. For a completely energy-neutral trajectory, one must have $\mathcal{S} = \mathcal{D}$ on average over the trajectory. In other words, if the soaring power $\mathcal{S}$ can be manipulated to contribute energy to the system, energy-neutral flight can be achieved.

The next question is how to manipulate the soaring power $\mathcal{S}$ to increase or maintain the system energy over the course of a flight cycle. Define first

$$\mathcal{S}_{\text{slope}} \triangleq -mgw_z \tag{2.12a}$$

$$\mathcal{S}_{\text{dyn}} \triangleq m\dot{\boldsymbol{v}}^\intercal \boldsymbol{w} \tag{2.12b}$$

$\mathcal{S}_{\text{slope}}$ denotes the energy gained due to either slope soaring or thermal soaring, where an updraft in wind, where $w_z < 0$ (remember the NED frame), will increase the energy of the system. A downdrift in wind will equally cause a decrease in the energy of the system.

$\mathcal{S}_{\text{dyn}}$ on the other hand, corresponds to the energy gained due to dynamic soaring. It is possible to expand this term further:

$$m\frac{d}{dt}(\boldsymbol{v}^\intercal \boldsymbol{w}) = m\dot{\boldsymbol{v}}^\intercal \boldsymbol{w} + m\boldsymbol{v}^\intercal \dot{\boldsymbol{w}} \tag{2.13}$$

$$\implies \mathcal{S}_{\text{dyn}} = m\frac{d}{dt}(\boldsymbol{v}^\intercal \boldsymbol{w}) - m\boldsymbol{v}^\intercal \dot{\boldsymbol{w}} \tag{2.14}$$

As stated in the opening, we only care about the net energy gain over one flight cycle. By requiring periodic motion, i.e. $\boldsymbol{v}(0) = \boldsymbol{v}(T)$ and $z(0) = z(T) \implies \boldsymbol{w}(z(0)) =$

$\boldsymbol{w}(z(T))$, and by integrating $\mathcal{S}_{\text{dyn}}$ over a flight cycle period T, one obtains

$$\begin{aligned}\frac{1}{T}\int_0^T \mathcal{S}_{\text{dyn}}\, d\tau &= \frac{1}{T}\int_0^T m\frac{d}{dt}\left(\boldsymbol{v}^\intercal \boldsymbol{w}\right)\, d\tau + \frac{1}{T}\int_0^T \left(-m\boldsymbol{v}^\intercal \dot{\boldsymbol{w}}\right)\, d\tau \\ &= \frac{1}{T}\int_0^T \left(-m\boldsymbol{v}^\intercal \dot{\boldsymbol{w}}\right)\, d\tau \end{aligned} \tag{2.15}$$

where the integral of the first term disappears due to the periodicity of the flight path. This means that it is only the second term $-m^\intercal \dot{\boldsymbol{w}}$ that can actually contribute net energy to the system over the course of a flight cycle. Let us thus define an active and a passive part of the soaring power:

$$\mathcal{S}_{\text{dyn,active}} \triangleq -m\boldsymbol{v}^\intercal \dot{\boldsymbol{w}} \tag{2.16a}$$

$$\mathcal{S}_{\text{dyn,passive}} \triangleq m\frac{d}{dt}(\boldsymbol{v}^\intercal \boldsymbol{w}) \tag{2.16b}$$

Now, take a look at the wind model, $\boldsymbol{w} = \boldsymbol{w}(h(t))$. Assume that the Jacobian of the wind model takes the form

$$\frac{\partial \boldsymbol{w}}{\partial h} = g(h)\boldsymbol{w}, \quad \text{where} \quad h > 0 \implies g(h) > 0 \tag{2.17}$$

such that

$$\dot{\boldsymbol{w}} = \frac{\partial \boldsymbol{w}}{\partial h}\dot{h} = g(h)\dot{h}\boldsymbol{w} \tag{2.18}$$

In that case, one has

$$\mathcal{S}_{\text{dyn,active}} = -m\boldsymbol{v}^\intercal \dot{\boldsymbol{w}} = -k\dot{h}\boldsymbol{v}^\intercal \boldsymbol{w} \tag{2.19}$$

where $k \triangleq mg(h) > 0$ is a strictly positive quantity for $h > 0$. From this, it follows that the active soaring power $\mathcal{S}_{\text{dyn,active}}$ is only positive for $\dot{h}\boldsymbol{v}^\intercal \boldsymbol{w} < 0$. As energy through soaring flight only enters the system through $\mathcal{S}_{\text{dyn}}$, and it is only the active soaring power that contributes energy over the course of a flight cycle, it suffices to say that $\dot{h}\boldsymbol{v}^\intercal \boldsymbol{w} < 0$ is the only way to supply the system with a net positive energy.

In summary, the following scenarios describe the only two ways the system can

gain energy from dynamic soaring:

- $\boldsymbol{v}^\intercal \boldsymbol{w} > 0$ and $\dot{h} < 0$: The system gains energy by **diving with** the wind.
- $\boldsymbol{v}^\intercal \boldsymbol{w} < 0$ and $\dot{h} > 0$: The system gains energy by **rising against** the wind.

This conclusion is consistent with Bower's result in [4], but generalizes to any 3-DOF point mass model. Take note that this result is in agreement with the original theory by Lord Rayleigh that states that energy is gained by flying with the wind where the wind is strongest [2], in the case where the wind increases with the height of the glider. However, this analysis also generalizes to wind fields where this is not necessarily the case.

The analysis performed here generalizes to a broad case of complex wind models and glider models, without going into details on either how the generation of aerodynamic forces are modelled or to the specifics of the aircraft. As will be shown in section 3.6, all of the wind models typically used in the context of dynamic soaring fall into the class described by eq. (2.17). To the knowledge of the author, the harvesting of energy through dynamic soaring has not previously been described by such a simple relationship that is presented in this chapter.

Chapter 3

Modeling

When researching autonomous dynamic soaring, a model of both the behaviour of an UAV and a model of the wind field is used. To reduce the problem complexity, it is common to neglect the UAVs rotational dynamics, arriving at a 3-DOF point mass model describing only the translational motion of the aircraft. Traditionally, such a 3-DOF model is often arrived at by using Newtons Second Law of Motion in combination with forward kinematics and Euler angles. One commonly assumes that the bank angle and the glider's ability to generate lift can be controlled directly, which, through the low-level control of control surfaces like the ailerons, elevators and the rudder, is often a fair assumption.

However, these traditional models seldom provide an intuitive understanding of flight through a wind field. With this in mind, a new model will be derived in this chapter, aimed at describing the complex motion of a glider in a wind field through simple algebraic relationships. In fact, a polynomial model, void of trigonometric terms and singularities, will be found. To further increase the intuitive meaning of the model, it will be reformulated to only depend on a single physical parameter, namely the lift-to-drag, or glide ratio, of the aircraft.

In addition to the aircraft model, at the end of the chapter, a quick overview of the different models that are typically used to describe wind fields will be covered. The one that most closely resembles real wind in the Earth's atmosphere is chosen for the experiments.

3.1 Glider Dynamics

The dynamics of a fixed-wing glider are usually described by two different models: by a three dimensional point-mass model, or an elaborate 6-DOF model. As stated in the opening, it is common to use the 3-DOF model in the context of dynamic soaring. The main advantage of using the 3-DOF model is computational efficiency, but this comes at the cost of lower accuracy. On the other hand, the 6-DOF model provides considerable more accuracy, at the cost of being more computationally expensive [13]. For reference, a A 3-DOF model is utilized in [3, 4, 7, 9, 10, 11, 12, 19, 21, 22], while a 6-DOF model is used in [15].

In this thesis, two different 3-DOF models will be considered. The 3-DOF point-mass model that is used by Zhao in [7] will be investigated. This model utilizes Euler angles, and therefore suffers from singularities. In the hopes of gaining more insight into the challenge of dynamic soaring, a new model will be proposed, under the name of the *Zhukovskii Glider*. It will be shown how this model can be arrived at through the use of simple aerodynamic principles, and how the new model is singularity-free. Finally, the similarity transformation between the two models will be derived, showing how the Zhukovskii Glider in fact captures the same dynamics as Zhao's model, without encountering singularities.

3.1.1 Forces Acting on a Glider

There are two sets of forces acting on a fixed-wing glider flying through a wind field: a gravitational force and an aerodynamic force.

In order to easily model the gravitational and aerodynamic forces acting on a glider, two different coordinate frames are introduced: the inertial NED frame and the wind frame. Let $\mathcal{N}$ denote the NED frame, and $\mathcal{W}$ denote the wind frame. The rotation from $\mathcal{N}$ to $\mathcal{W}$ consists of a series of consecutive Euler rotations: a rotation of the air-relative heading ψ around the z-axis, a rotation of the air-relative flight path angle γ around the resulting y-axis, and then a rotation of the bank angle ϕ around

the resulting x-axis. This rotation can be described by the following rotation matrix:

$$\boldsymbol{R}_W^N = \boldsymbol{R}_z(\psi)\boldsymbol{R}_y(\gamma)\boldsymbol{R}_x(\phi) \tag{3.1}$$

$$= \begin{bmatrix} \mathrm{c}_\psi \mathrm{c}_\gamma & \mathrm{c}_\psi \mathrm{s}_\gamma \mathrm{s}_\phi - \mathrm{s}_\psi \mathrm{c}_\phi & \mathrm{c}_\psi \mathrm{s}_\gamma \mathrm{c}_\phi + \mathrm{s}_\psi \mathrm{s}_\phi \\ \mathrm{s}_\psi \mathrm{c}_\gamma & \mathrm{s}_\psi \mathrm{s}_\gamma \mathrm{s}_\phi + \mathrm{c}_\psi \mathrm{c}_\phi & \mathrm{s}_\psi \mathrm{s}_\gamma \mathrm{c}_\phi - \mathrm{c}_\psi \mathrm{s}_\phi \\ -\mathrm{s}_\gamma & \mathrm{c}_\gamma \mathrm{s}_\phi & \mathrm{c}_\gamma \mathrm{c}_\phi \end{bmatrix} \triangleq \begin{bmatrix} \hat{\mathbf{i}}_W & \hat{\mathbf{j}}_W & \hat{\mathbf{k}}_W \end{bmatrix} \tag{3.2}$$

where $\hat{\mathbf{i}}_W, \hat{\mathbf{j}}_W$ and $\hat{\mathbf{k}}_W$ are the unit vectors describing the wind frame $\mathcal{W}$. In this chosen reference frame, $\hat{\mathbf{i}}_W$ lies along the airspeed of the glider, $\hat{\mathbf{j}}_W$ vector lies along the wingspan of the glider, and $\hat{\mathbf{k}}_W$ is normal to the two proceeding vectors. Let $\boldsymbol{e}_x$, $\boldsymbol{e}_y$ and $\boldsymbol{e}_z$ be the unit vectors describing the NED frame $\mathcal{N}$. In fig. 3-1, the $\mathcal{N}$ frame and the $\mathcal{W}$ frame are illustrated.

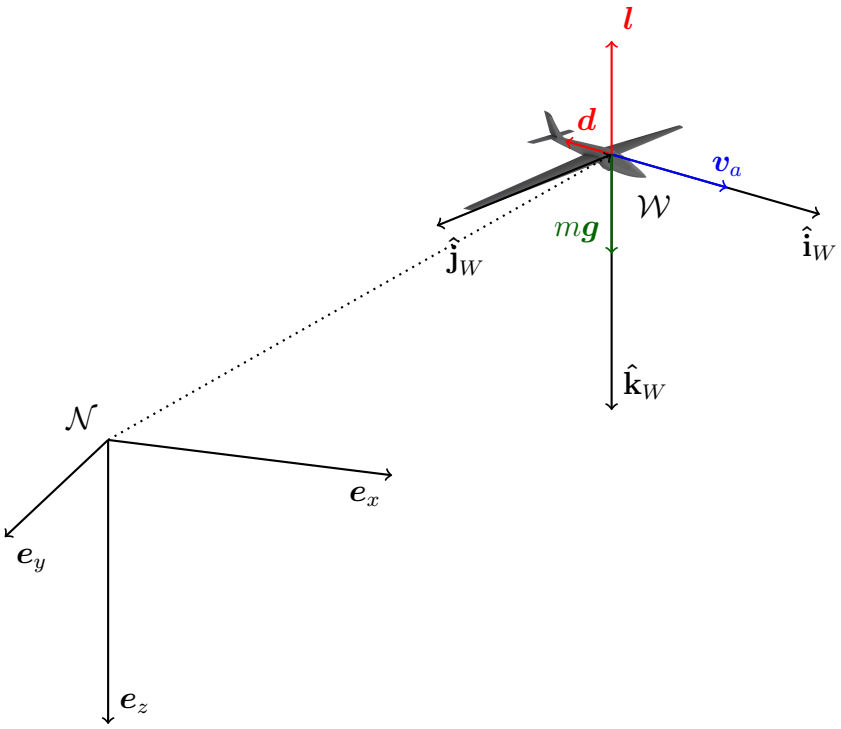

Figure 3-1: Coordinate frames and forces acting on a glider

The gravitational force is working in the NED frame $\mathcal{N}$, and is given by $m\boldsymbol{g}$, with $\boldsymbol{g} = 9.81\boldsymbol{e}_z$. The definition of the wind frame $\mathcal{W}$ lets us easily define the drag force as $\boldsymbol{d} = -|\boldsymbol{d}|\hat{\mathbf{i}}_W$, and the lift force as $\boldsymbol{l} = -|\boldsymbol{l}|\hat{\mathbf{k}}_W$. It should also be noted that this

definition of the $\mathcal{W}$ frame means that $\hat{\mathbf{j}}_W$ is aligned with the wing-span of the glider. This frame of reference is adapted from [26]. The coordinate frames, as well as the forces acting on a glider, can be seen in fig. 3-1.

Following quasi-steady flight dynamics, the lift and drag are specified according to

$$D \triangleq |\boldsymbol{d}| = \frac{1}{2}\rho A c_D |\boldsymbol{v}_a|^2 \tag{3.3a}$$

$$L \triangleq |\boldsymbol{l}| = \frac{1}{2}\rho A c_L |\boldsymbol{v}_a|^2 \tag{3.3b}$$

where c_D and c_L are the drag and lift coefficients, A is the surface area of the wing, ρ is the air density, and $\boldsymbol{v}_a = \boldsymbol{v} - \boldsymbol{w}$ is the airspeed of the glider, with $\boldsymbol{v}$ being the inertial speed of the glider, and $\boldsymbol{w} = \boldsymbol{w}(h(t))$ being the wind speed. A visualization of the wind triangle can be seen in fig. 3-2.

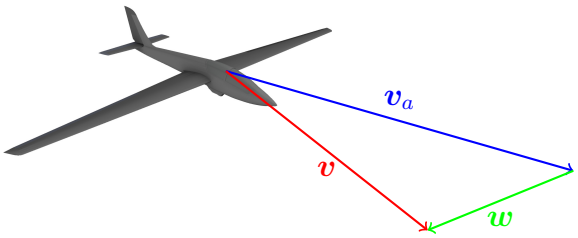

Figure 3-2: Wind triangle, showing the relation between the airspeed $\boldsymbol{v}_a$, inertial speed $\boldsymbol{v}$ and wind speed $\boldsymbol{w}$.

3.2 Zhao's Model

The 3-DOF point-mass model conventionally used in other relevant work on dynamic soaring was first introduced by Zhao et al. in [27], and used in the context of dynamic soaring in [7]. It will be referred to as Zhao's model. In [4, 13], it is shown how Zhao's model can be transformed to the model introduced by Sachs in [3, 22]. As most researchers use either the model from Zhao or from Sachs, it is deemed relevant to describe these models in this work. Zhao's dynamics will thus be derived and

explained in this section, and as Zhao's model has been shown to be identical to Sachs' model, Sachs' model will not be mentioned again. Later, it will be shown how the Zhukovskii Glider relates to Zhao's, and hence also Sachs', model.

Using Newtons second law of motion for a point mass influenced by the forces as described in section 3.1.1, one gets:

$$m\dot{\boldsymbol{v}} = m\boldsymbol{g} - L\hat{\mathbf{k}}_W - D\hat{\mathbf{i}}_W \tag{3.4}$$

which, using $\boldsymbol{R}_W^N$ defined in eq. (3.2), gives:

$$m\ddot{x} = -D\cos\gamma\cos\psi + L(-\sin\gamma\cos\psi\cos\phi - \sin\psi\sin\phi) \tag{3.5a}$$

$$m\ddot{y} = -D\cos\gamma\sin\psi + L(-\sin\gamma\sin\psi\cos\phi - \cos\psi\sin\phi) \tag{3.5b}$$

$$m\ddot{z} = -D\sin\gamma + L(-\cos\gamma\cos\phi) + mg \tag{3.5c}$$

Given the airspeed $V_a \triangleq |\boldsymbol{v}_a|$ and the wind $\boldsymbol{w}$, the kinematics for a glider are given by

$$\dot{\boldsymbol{p}} = \boldsymbol{v} = V_a\hat{\mathbf{i}}_W + \boldsymbol{w}(h(t)) \tag{3.6}$$

which, when written out, gives

$$\dot{x} = V_a\cos\gamma\cos\psi + w_x(h(t)) \tag{3.7a}$$

$$\dot{y} = V_a\cos\gamma\sin\psi + w_y(h(t)) \tag{3.7b}$$

$$\dot{z} = -V_a\sin\gamma + w_z(h(t)) \tag{3.7c}$$

In Zhao's model, the state vector consists of $\boldsymbol{x} = [V_a, \psi, \gamma, x, y, z]$. In order to arrive at these dynamics, the kinematics in eq. (3.7) are differentiated with respect to time, and plugged into the equations given by eq. (3.5). Solving the resulting equations for

$\dot{V}_a, \dot{\psi}, \dot{\gamma}$, one obtains the dynamics:

$$m\dot{V}_a = -D - mg\sin\gamma - m\dot{w}_x\cos\gamma\cos\psi - m\dot{w}_y\cos\gamma\sin\psi + m\dot{w}_z\sin\gamma \tag{3.8a}$$

$$mV_a\dot{\gamma} = -L\cos\phi - mg\cos\gamma + m\dot{w}_x\sin\gamma\cos\psi + m\dot{w}_y\sin\gamma\sin\psi + m\dot{w}_z\cos\gamma \tag{3.8b}$$

$$mV_a\dot{\psi}\cos\gamma = L\sin\phi + m\dot{w}_x\sin\psi - m\dot{w}_y\cos\psi \tag{3.8c}$$

$$\dot{x} = V_a\cos\gamma\cos\psi + w_x \tag{3.8d}$$

$$\dot{y} = V_a\cos\gamma\sin\psi + w_y \tag{3.8e}$$

$$\dot{z} = -V_a\sin\gamma + w_z \tag{3.8f}$$

with the lift and drag force given as defined in eq. (3.3). The drag is assumed to be quadratic, such that $c_D = c_{D,0} + kc_L^2$, where $c_{D,0}$ corresponds to the parasitic drag generated when there is no lift, and k expresses the additional generation of drag due to lift. Note that the model becomes a lot simpler by assuming that the wind always blows along either the x or the y-axis, which can always be achieved through a change in coordinates.

The lift coefficient and the roll angle are chosen as inputs, that is, $\boldsymbol{u} = [c_L, \phi]$, under the assumption that any (reasonable) $\boldsymbol{u}$ may be generated over short time scales, by appropriately adjusting the control surfaces of the glider. As stated in the opening of this chapter, this model uses Euler angles, and hence has problems with singularities. Singularities are encountered when $V_a = 0$, $\gamma = \frac{1}{2}\pi$ or $\gamma = \frac{3}{2}\pi$.

3.3 The Zhukovskii Glider

3.3.1 Basic Derivation

In this section, a new, polynomial, singularity-free, model for the motion of a point mass glider is proposed. By deriving what appears to be a simpler and more intuitive model through fundamental principles of aerodynamics, the author hopes to provide

additional insight into the challenge of dynamic soaring. The derivation follows the work done by this thesis' supervisor, Morten D. Pedersen, in his technical note [25].

Once again, the general motion of a point mass influenced by a gravitational force and the aerodynamic forces $\boldsymbol{f} = \boldsymbol{l} + \boldsymbol{d}$ is described by

$$m\dot{\boldsymbol{v}} = m\boldsymbol{g} + \boldsymbol{f} \tag{3.9}$$

The simplest model that can capture the orthogonality of lift and relative flow, i.e. $\boldsymbol{v}_a \perp \boldsymbol{l}$, is found in the so-called vortex lifting law [28] as proposed by Nikolay Zhukovskii:

$$\boldsymbol{l} = \rho \boldsymbol{S}(\boldsymbol{c})\boldsymbol{v}_a \tag{3.10}$$

where $\boldsymbol{c}$ denotes the net circulation along the lifting line of the wing, and $\boldsymbol{S}(\cdot)$ denotes the skew symmetric matrix that lets us describe the cross product between two vectors as the product between a matrix and a vector, as introduced in [29].

Further, it will be assumed that there is no sideslip of the glider, i.e. that the glider is always aligned with the airspeed vector $\boldsymbol{v}_a$, and that the wings lifting line is therefore always perpendicular to the airspeed of the glider. That is,

$$\boldsymbol{v}_a \perp \boldsymbol{c} \tag{3.11}$$

The drag is parallel to the relative flow, i.e. $\boldsymbol{d} \parallel \boldsymbol{v}_a$, and the simplest expression that captures this is given by

$$\boldsymbol{d} = -\rho d \boldsymbol{v}_a, \quad d = \frac{1}{2} A c_D |\boldsymbol{v}_a| \tag{3.12}$$

where d is simply a parameter that is given by the choice of the drag model in eq. (3.3a), such that $\boldsymbol{d} = -\frac{1}{2}\rho A c_D |\boldsymbol{v}_a| \boldsymbol{v}_a$

The drag is modelled as two individual parts, a parasitic part and an induced part $c_D = c_{D,p} + c_{D,i}$. By utilizing Lifting Line Theory and by assuming a wing with elliptical span loading and aspect ratio $\text{Æ} = \frac{b^2}{A}$ as done in [24], where b denotes the

wingspan, the induced drag coefficient may be expressed in terms of the wings lift coefficient c_L with

$$c_{D,i} = \frac{c_L^2}{\pi \mathit{Æ}} = \frac{|\boldsymbol{l}|^2}{\pi \mathit{Æ}(\frac{1}{2}\rho A|\boldsymbol{v_a}|^2)^2} \tag{3.13}$$

where the definition of lift in eq. (3.3b) has been used.

The magnitude of the lift vector can be found as

$$\begin{aligned} |\boldsymbol{l}| = \sqrt{\boldsymbol{l}^\intercal \boldsymbol{l}} &= \rho\sqrt{\boldsymbol{v}_a^\intercal \boldsymbol{S}(\boldsymbol{c})^\intercal \boldsymbol{S}(\boldsymbol{c})\boldsymbol{v}_a} \\ &= \rho\sqrt{-\boldsymbol{v}_a^\intercal \boldsymbol{S}(\boldsymbol{c})^2 \boldsymbol{v}_a} = \rho\sqrt{-\boldsymbol{v}_a^\intercal (\boldsymbol{c}\boldsymbol{c}^\intercal - \boldsymbol{c}^\intercal \boldsymbol{c}\boldsymbol{I})\boldsymbol{v}_a} \\ &= \rho|\boldsymbol{c}||\boldsymbol{v}_a| \end{aligned} \tag{3.14}$$

where the fact that $\boldsymbol{c}^\intercal \boldsymbol{v}_a = 0$ and the definition of the vector triple product is used. This lets us formulate the induced drag $c_{D,i}$ in terms of the net circulation over the wing:

$$c_{D,i} = \frac{4|\boldsymbol{c}|^2}{\pi \mathit{Æ} A^2 |\boldsymbol{v_a}|^2} \tag{3.15}$$

This leaves us with the following, complete, 3-DOF model for the glider, hereby referred to as the *Zhukovskii Glider*:

$$m\dot{\boldsymbol{v}} = -\rho(d\boldsymbol{I} + \boldsymbol{S}(\boldsymbol{c}))\boldsymbol{v}_a + m\boldsymbol{g} \tag{3.16a}$$

$$\dot{\boldsymbol{p}} = \boldsymbol{v} \tag{3.16b}$$

with

$$d = \frac{1}{2}A|\boldsymbol{v}_a|c_{D,p} + \frac{2|\boldsymbol{c}|^2}{\pi \mathit{Æ} A|\boldsymbol{v}_a|} \tag{3.17}$$

where $c_{D,p}$, A and $\mathit{Æ} = \frac{b^2}{A}$ are physical constants of the glider as defined previously. The state vector consists of the position and velocity of the glider, $\boldsymbol{x} = [\boldsymbol{p}^\intercal, \boldsymbol{v}^\intercal]^\intercal = [x, y, z, \dot{x}, \dot{y}, \dot{z}]^\intercal$, and the relative velocity is given by $\boldsymbol{v}_a = \boldsymbol{v} - \boldsymbol{w}$. The input is chosen as $\boldsymbol{u} = \boldsymbol{c}$, under the assumption that any $\boldsymbol{c}$ that is perpendicular to $\boldsymbol{v}_a$ may be generated by the lifting surface of the glider over short time scales, once again by appropriately adjusting the control surfaces of the glider.

Note that by avoiding the use of Euler angles entirely, the model does not en-

counter any problems with singularities related to the attitude of the glider. However, as with Zhao's dynamics defined in the previous section, this model is not defined when the airspeed is zero, $V_a = |\boldsymbol{v}_a| = 0$.

3.3.2 Performance Parameters

When talking about gliders, it is common to use specific performance parameters. These parameters will come in handy for greatly simplifying the glider model, and this subsection will introduce these parameters.

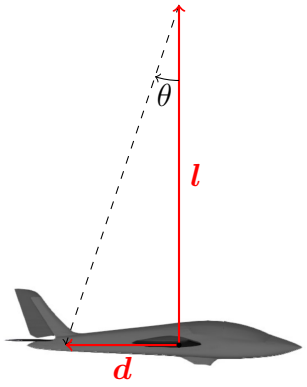

Figure 3-3: Visualization of the lift-to-drag ratio.

The first of these parameters is the glide ratio λ, also known as finesse or glide number, which corresponds to the lift-to-drag ratio:

$$\lambda = \frac{L}{D} = \frac{1}{\tan\theta} \tag{3.18}$$

where θ is the current glide angle of the glider. A visualization of the lift-to-drag ratio can be seen in fig. 3-3.

The glide ratio will vary with lift and drag, and also describes the ratio of horizontal speed to altitude loss, a relationship that will soon be proven. It is common to talk about an optimal glide ratio $\Lambda \triangleq \lambda_{\text{opt}}$ and the optimal glide angle $\Theta \triangleq \theta_{\text{opt}}$. Another performance parameter that is common is the optimal glide speed V_{opt}. This is the speed at which the glider will glide passively at the optimal glide ratio, i.e. at the optimal glide angle.

First, we seek a general expression for the glide ratio in steady flight, in the case where there is no wind. During steady flight, the acceleration of the vehicle will be zero $\dot{\boldsymbol{v}} = \mathbf{0}$, which gives $\boldsymbol{f} = -m\boldsymbol{g} = -mg\boldsymbol{e}_z$. In addition to this, we look at the case where there is no wind, such that $\boldsymbol{v_a} = \boldsymbol{v}$. The drag is given as the projection of the aerodynamic force vector $\boldsymbol{f}$ on the airspeed $\boldsymbol{v}_a = \boldsymbol{v}$

$$\boldsymbol{d} = \frac{\boldsymbol{v}\boldsymbol{v}^\intercal}{|\boldsymbol{v}|^2}\boldsymbol{f} = -mg\frac{\boldsymbol{v}\boldsymbol{v}^\intercal}{|\boldsymbol{v}|^2}\boldsymbol{e}_z = mg\frac{\boldsymbol{v}\dot{h}}{|\boldsymbol{v}|^2} \tag{3.19}$$

$$\implies |\boldsymbol{d}| = mg\frac{|\dot{h}|}{|\boldsymbol{v}|} \tag{3.20}$$

where $\boldsymbol{v}^\intercal\boldsymbol{e}_z = -\dot{h}$. The lift is then given as follows:

$$\boldsymbol{l} = \boldsymbol{f} - \boldsymbol{d} = -mg(\boldsymbol{e_z} + \frac{\boldsymbol{v}\dot{h}}{|\boldsymbol{v}|^2}) \tag{3.21}$$

$$\implies |\boldsymbol{l}| = \sqrt{\boldsymbol{l}^\intercal\boldsymbol{l}} = mg\sqrt{1 - \left(\frac{\dot{h}}{|\boldsymbol{v}|}\right)^2} \tag{3.22}$$

The glide ratio follows as the lift-to-drag

$$\lambda = \frac{|\boldsymbol{l}|}{|\boldsymbol{d}|} = \frac{\sqrt{|\boldsymbol{v}|^2 - |\dot{h}|^2}}{|\dot{h}|} = \frac{|\boldsymbol{v}_{\text{hor}}|}{|\dot{h}|} \tag{3.23}$$

This expression shows why the glide ratio corresponds to the ratio of horizontal speed to altitude loss, as mentioned in the beginning. This physical interpretation can also be seen for an aircraft gliding passively in fig. 3-4.

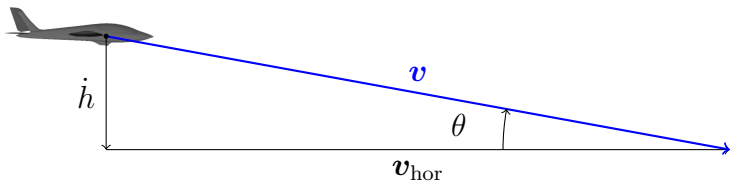

Figure 3-4: Physical interpretation of the glide ratio.

We now seek to relate this lift-to-drag ratio to our model. The norm of the lift

vector gives $|\boldsymbol{l}| = \rho|\boldsymbol{c}||\boldsymbol{v}_a|$ as shown in eq. (3.14). Thus, the circulation is found as

$$|\boldsymbol{c}| = \frac{|\boldsymbol{l}|}{\rho|\boldsymbol{v}|} = \frac{mg\sqrt{1-(\frac{|\dot{h}|}{|\boldsymbol{v}|})^2}}{\rho|\boldsymbol{v}|} \tag{3.24}$$

Using this and following the definition of drag given in eq. (3.17) gives the total drag

$$|\boldsymbol{d}| = \rho d|\boldsymbol{v}| = \rho\left(\frac{1}{2}A|\boldsymbol{v}|^2 c_{D,p} + \frac{2(mg)^2(1-(\frac{|\dot{h}|}{|\boldsymbol{v}|})^2)}{\pi \mathcal{R} A \rho^2 |\boldsymbol{v}|^2}\right) \tag{3.25}$$

One then obtains the following glide ratio in terms of the model parameters

$$\lambda = \frac{|\boldsymbol{l}|}{|\boldsymbol{d}|} = \frac{1}{\frac{1}{2}c_{D,p}\sigma + \frac{2}{\pi\mathcal{R}}\frac{1}{\sigma}} \tag{3.26}$$

with $\sigma \triangleq \frac{\rho A|\boldsymbol{v}|^2}{mg\sqrt{1-(\frac{|\dot{h}|}{|\boldsymbol{v}|})^2)}}$ defined to simplify notation.

To find the optimal glide ratio, consider for a moment the function

$$f(x) = \frac{1}{ax + \frac{b}{x}} \tag{3.27}$$

which reaches its maximum at $f(x) = \frac{1}{2}\frac{1}{\sqrt{ab}}$ when $x = +\sqrt{\frac{b}{a}}$, for $ab > 0$. The function is visualized in fig. 3-5.

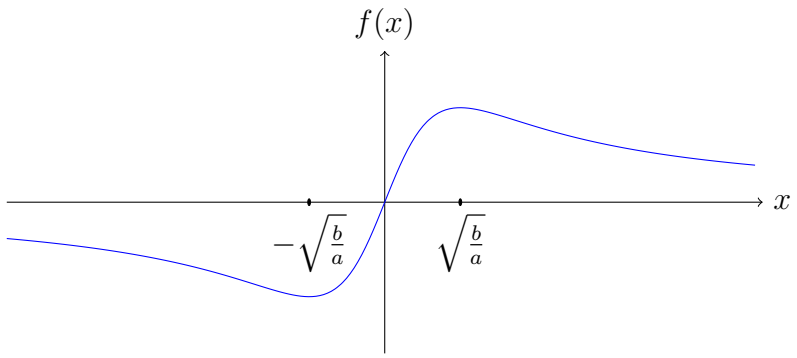

Figure 3-5: Function from eq. (3.27)

Using this, the maximum glide ratio is found as

$$\Lambda = \frac{1}{2}\sqrt{\frac{\pi \mathit{A\!R}}{c_{D,p}}} \tag{3.28}$$

$$\text{when} \quad \sigma = \frac{\rho A|\boldsymbol{v}|^2}{mg\sqrt{1-(\frac{|\dot{h}|}{|\boldsymbol{v}|})^2)}} = \frac{2}{\sqrt{\pi \mathit{A\!R} c_{D,p}}} \tag{3.29}$$

Next, we proceed to define the glide angle and the glide speed. Geometrically, the glide angle θ is defined in terms of the glide ratio as $\lambda = \frac{1}{\tan\theta}$, which can be seen in fig. 3-3. From eq. (3.23) the following relationship is found

$$\frac{|\dot{h}|}{|\boldsymbol{v}|} = \sin\theta \tag{3.30}$$

which can readily be seen by looking at the vertical and horizontal components of the velocity vector $\boldsymbol{v}$ in figure fig. 3-4. Let $\Theta \triangleq \theta_{\text{opt}}$ denote the glide angle at the optimal glide ratio Λ.

The relationship in eq. (3.29) gives a mean of calculating the optimal glide speed $V_{\text{opt}} = |\boldsymbol{v}_{\text{opt}}|$, given the optimal glide angle Θ

$$\begin{aligned} \frac{\rho A V_{\text{opt}}^2}{mg\sqrt{1-(\frac{|\dot{h}|}{|\boldsymbol{v}|})^2)}} &= \frac{\rho A V_{\text{opt}}^2}{mg\cos\Theta} = \frac{2}{\sqrt{\pi \mathit{A\!R} c_{D,p}}} \\ \implies V_{\text{opt}} &= \sqrt{\frac{2mg\cos\Theta}{\sqrt{\pi \mathit{A\!R} c_{D,p}}\rho A}} = \sqrt{\frac{2mg\cos\Theta}{\sqrt{\pi c_{D,p} A}b\rho}} \end{aligned} \tag{3.31}$$

To summarize, eq. (3.28) and eq. (3.31) now provides a way of calculating the performance parameters Λ and V_{opt} given the glider parameters $c_{D,p}$, A and $\mathit{A\!R} = \frac{b^2}{A}$. A straight forward inversion of the equations give

$$\pi \mathit{A\!R} = \frac{4mg}{\rho A V_{\text{opt}}^2}\frac{\Lambda^2}{\sqrt{1+\Lambda^2}}, \quad \text{or } b = \sqrt{\frac{4mg}{\pi\rho V_{\text{opt}}^2}\frac{\Lambda^2}{\sqrt{1+\Lambda^2}}} \tag{3.32a}$$

$$c_{D,p} = \frac{mg}{\rho A V_{\text{opt}}^2}\frac{1}{\sqrt{1+\Lambda^2}} \tag{3.32b}$$

which gives a mean for calculating the required wingspan b and the parasitic drag

coefficient $c_{D,p}$, given the optimal glide ratio Λ, the optimal glide speed V_{opt} and the effective surface area of the glider A.

The relationship between the model parameters and the performance parameters in eq. (3.32) is then used to reparametrize the model drag as

$$\begin{aligned}\boldsymbol{d} &= -\frac{1}{2}mg\left(\frac{1}{\sqrt{1+\Lambda^2}}\left(\frac{|\boldsymbol{v_a}|}{V_{\text{opt}}}\right)^2 + \frac{\sqrt{1+\Lambda^2}}{\Lambda^2}\left(\frac{\rho|\boldsymbol{c}|V_{\text{opt}}}{mg}\right)^2\right)\frac{\boldsymbol{v}_a}{|\boldsymbol{v}_a|} \\ &= -\frac{1}{2}mg\sin\Theta\left(\left(\frac{|\boldsymbol{v_a}|}{V_{\text{opt}}}\right)^2 + \left(\frac{\rho|\boldsymbol{c}|V_{\text{opt}}}{mg\cos\Theta}\right)^2\right)\frac{\boldsymbol{v}_a}{|\boldsymbol{v}_a|} = -\rho d\boldsymbol{v_a} \qquad (3.33)\end{aligned}$$

where the fact that $\cos^2\Theta = \frac{\Lambda^2}{\sqrt{1+\Lambda^2}}$, which comes from squaring eq. (3.23), has been used.

3.3.3 Performance Parameters in Steady, Level Flight

It turns out that the parameters defining the behaviour of the glider in steady, *level* flight in the case of no wind, allows the number of model parameters to be reduced significantly. As before, zero wind gives $\boldsymbol{v}_a = \boldsymbol{v}$.

In steady, level flight, the acceleration will be zero, as in the case with non-level flight. However, because of the level flight, the lift will be the only force counteracting the gravitational force acting on the glider, hence $|\boldsymbol{l}| = mg \implies |\boldsymbol{c}| = \frac{|\boldsymbol{l}|}{\rho|\boldsymbol{v}|} = \frac{mg}{\rho|\boldsymbol{v}|}$. Combining this with the result from eq. (3.33), the glide ratio now reads as

$$\lambda = \frac{|\boldsymbol{l}|}{|\boldsymbol{d}|} = \frac{1}{\frac{1}{2}\sin\Theta}\frac{1}{\left(\frac{1}{V_{\text{opt}}^2}|\boldsymbol{v}|^2 + \frac{V_{\text{opt}}^2}{\cos^2\Theta}\frac{1}{|\boldsymbol{v}|^2}\right)} \qquad (3.34)$$

If the reader finds it odd that the optimal glide ratio at level flight seems to include a non-zero glide angle, then it should be recalled that Θ defines the *optimal* glide angle Λ defined in the previous section, which is a constant that has nothing to do with level flight. The new function for the glide ratio in eq. (3.34) is a function of the same form as in eq. (3.27). From this, the maximum glide ratio is found to be

the same value as before, $\Lambda_{\text{level}} = \Lambda$. However, the optimal glide speed is reached at

$$V_l = \frac{V_{\text{opt}}}{\sqrt{\cos\Theta}}, \quad \implies V_{\text{opt}} = V_l \cos\Theta \tag{3.35}$$

which for $\Theta < 90°$ will be slightly faster than the glide speed in steady non-level flight V_{opt}.

By replacing all instances of the optimal glide speed V_{opt} with the optimal glide speed in level flight V_l, the drag in eq. (3.33) can be further simplified as

$$\begin{aligned}
\boldsymbol{d} &= -\frac{1}{2} mg \tan\Theta \left(\left(\frac{|\boldsymbol{v_a}|}{V_l} \right)^2 + \left(\frac{\rho |\boldsymbol{c}| V_l}{mg} \right)^2 \right) \frac{\boldsymbol{v}_a}{|\boldsymbol{v}_a|} \\
&= -\frac{mg}{2\Lambda |\boldsymbol{v}_a|} \left(\left(\frac{|\boldsymbol{v_a}|}{V_l} \right)^2 + \left(\frac{\rho |\boldsymbol{c}| V_l}{mg} \right)^2 \right) \boldsymbol{v_a} \\
&= -\rho d \boldsymbol{v}_a, \quad d \triangleq \frac{mg}{\rho \Lambda V_l} l \left(\frac{|\boldsymbol{v_a}|}{V_l}, \frac{\rho V_l |\boldsymbol{c}|}{mg} \right)
\end{aligned} \tag{3.36}$$

where $l(a,b) \triangleq \frac{a^2+b^2}{2a}$ is defined to simplify the notation. $l(a,b)$ can also be interpreted as a natural loss function in the model. To summarize thus far, we now have the model of the glider as defined in eq. (3.16), but with the parameter d defined in terms of performance parameters as shown in eq. (3.36).

The last parameter that will be introduced is the characteristic circulation C, which corresponds to the total circulation required for steady, level flight at at the optimal glide speed. Under the conditions of steady, level flight, we have that $\dot{\boldsymbol{v}}_a = \boldsymbol{0}$, which inserted into the Zhukovskii Glider gives

$$0 = -\rho(d\boldsymbol{I} + \boldsymbol{S}(\boldsymbol{c}))\boldsymbol{v_a} + m\boldsymbol{g} \tag{3.37}$$

Taking the cross product with $\boldsymbol{v}_a$ yields

$$\begin{aligned} -m\boldsymbol{S}(\boldsymbol{v}_a)\boldsymbol{g} &= \rho\boldsymbol{S}(\boldsymbol{v}_a)^2\boldsymbol{c} \\ &= \rho(\boldsymbol{v}_a\boldsymbol{v}_a^\intercal - |\boldsymbol{v}_a|^2)\boldsymbol{c} = -\rho V_l^2\boldsymbol{c} \\ \implies \boldsymbol{c} &= \frac{m}{\rho V_l^2}\boldsymbol{S}(\boldsymbol{v}_a)\boldsymbol{g} \end{aligned} \tag{3.38}$$

Finally, taking the vector norm gives

$$C \triangleq |\boldsymbol{c}| = \frac{mg}{\rho V_l} \tag{3.39}$$

where the facts that $|\boldsymbol{v}_a| = V_l$ and $\boldsymbol{v}_a \perp \boldsymbol{g}$ due to the level flight assumption have been used. C will be referenced as the characteristic circulation of the glider.

3.3.4 Rescaling of the Model

It turns out that by using the performance parameters defined in the previous sections, the model can be further rescaled to only depend on a single physical parameter. A similar step is performed in [7] and [11]. However, in these formulations, parameters like the lift and drag coefficients still remain in the formulation of the dynamics. Here, the 3-DOF point-mass model will be reparametrized in a way such that it is only dependent on the optimal glide ratio Λ. In addition to this, normalizing the model improves its numerical properties, as stated in for example [7, 10, 11].

First, we define the characteristic length $L = \frac{V_l^2}{g}$ and the characteristic time $T = \frac{V_l}{g}$. We can now define the dimensionless variables

$$\bar{\boldsymbol{c}} = \frac{\boldsymbol{c}}{C}, \quad \bar{\boldsymbol{v}} = \frac{\boldsymbol{v}}{V}, \quad \bar{\boldsymbol{x}} = \frac{\boldsymbol{x}}{L}, \quad \bar{\boldsymbol{w}}(\bar{\boldsymbol{x}}) = \frac{1}{V_l}\boldsymbol{w}(L\boldsymbol{x}) \quad \dot{\bar{\boldsymbol{v}}}_r = \frac{\dot{\boldsymbol{v}}_r}{g}, \quad \bar{t} = \frac{t}{T} \tag{3.40}$$

substituting these dimensionless variables into the Zhukovskii Glider gives the

following, rescaled model

$$\dot{\boldsymbol{v}} + (\frac{1}{\Lambda} l(|\boldsymbol{v}_a|, |\boldsymbol{c}|)\boldsymbol{I} + \boldsymbol{S}(\boldsymbol{c}))\boldsymbol{v}_a = \boldsymbol{e}_z \tag{3.41a}$$

$$\dot{\boldsymbol{p}} = \boldsymbol{v} \tag{3.41b}$$

where $l(a,b) = \frac{a^2+b^2}{2a}$ and the notational bars have been omitted for simplicity. Because of the rescaling, this model is completely void of physical parameters, except for the optimal glide ratio of the glider Λ.

3.3.5 Relative Formulation

All aerodynamic effects rely solely on the relative airspeed $\boldsymbol{v}_a$ of the glider, rather than the inertial velocity $\boldsymbol{v}$. Hence, optimization constraints on all aerodynamic quantities are easier to implement if a reformulation of the dynamics is performed. The last step of the modeling is therefore to reformulate the model such that the state consists of the airspeed rather than the inertial velocity. As will be seen, this is a simple procedure.

First, by remembering $\boldsymbol{v}_a = \boldsymbol{v} - \boldsymbol{w}(\boldsymbol{p}(t))$, time differentiation gives

$$\dot{\boldsymbol{v}}_a = \dot{\boldsymbol{v}} - \left(\frac{\partial \boldsymbol{w}}{\partial t} + \frac{\partial \boldsymbol{w}}{\partial \boldsymbol{p}}\boldsymbol{v}\right) = \dot{\boldsymbol{v}} - \left(\frac{\partial \boldsymbol{w}}{\partial \boldsymbol{p}}\boldsymbol{v}_a + \frac{\partial \boldsymbol{w}}{\partial \boldsymbol{p}}\boldsymbol{w}\right) = \dot{\boldsymbol{v}} - \frac{\partial \boldsymbol{w}}{\partial \boldsymbol{p}}\boldsymbol{v}_a \tag{3.42}$$

The last equality comes from assuming that the wind field acts horizontally while being a function of just the altitude of the glider:

$$\frac{\partial \boldsymbol{w}}{\partial \boldsymbol{p}} = \begin{bmatrix} 0 & 0 & w_x(z(t)) \\ 0 & 0 & w_y(z(t)) \\ 0 & 0 & 0 \end{bmatrix} \implies \frac{\partial \boldsymbol{w}}{\partial \boldsymbol{p}}\boldsymbol{w} = \boldsymbol{0} \tag{3.43}$$

Hence, eq. (3.41) can be reformulated as

$$\dot{\boldsymbol{v}}_a + (\frac{1}{\Lambda} l(|\boldsymbol{v}_a|, |\boldsymbol{c}|)\boldsymbol{I} + \boldsymbol{S}(\boldsymbol{c}) + \frac{\partial \boldsymbol{w}}{\partial \boldsymbol{p}})\boldsymbol{v}_a = \boldsymbol{e}_z \tag{3.44a}$$

$$\dot{\boldsymbol{p}} = \boldsymbol{v}_a + \boldsymbol{w} \tag{3.44b}$$

with the new state $\boldsymbol{x} = [\boldsymbol{p}^\intercal, \boldsymbol{v}_a^\intercal]^\intercal$. Due to its simplicity, this is the model that will be used throughout the rest of this thesis.

3.4 Comparison Between the Models

3.4.1 Physical Equality

Zhao's dynamics and the *Zhukovskii Glider* differ in the derivation of aerodynamic forces, in the chosen state vector $\boldsymbol{x}$, and in the chosen input $\boldsymbol{u}$. In Zhao's model, the state vector is $\boldsymbol{x} = [V_a, \psi, \gamma, x, y, z]^\intercal$, with the input vector $\boldsymbol{u} = [c_L, \phi]^\intercal$. In the Zhukovskii Glider, the state is $\boldsymbol{x} = [x, y, z, \dot{x}, \dot{y}, \dot{z}]^\intercal$ and the input is $\boldsymbol{u} = \boldsymbol{c}$. This section will show that given a state-input pair $(\boldsymbol{x}, \boldsymbol{u})$ in one of the models, there exists a one-to-one mapping to the other model.

First, the physical similarities between the models will be shown, even though they are mathematically different and are derived from different aerodynamic perspectives. Starting with the drag force, the two models present two different parameterizations for the drag coefficients

$$c_D = c_{D,0} + \frac{1}{\pi \mathcal{R}} c_L^2 \tag{3.45a}$$

$$c_D = c_{D,0} + k c_L^2 \tag{3.45b}$$

By choosing $k = \frac{1}{\pi \mathcal{R}}$, the two models becomes equal. At the same time, one equips the constant with physical significance. With this k, the drag magnitudes $|\boldsymbol{d}| = D$ are equal between the models. Next, the drag force in Zhao's dynamics acts along the negative relative airspeed of the glider, or along $-\hat{\mathbf{i}}_W$. Since zero sideslip is assumed

in the Zhukovskii Glider, this gives $\hat{\mathbf{i}}_W = \frac{\boldsymbol{v}_a}{|\boldsymbol{v}_a|}$, which in turn shows that the drag forces are equal.

Moving on to the lift force, remember that we defined $\boldsymbol{l} = -L\hat{\mathbf{k}}_W = -\frac{1}{2}\rho A c_L |\boldsymbol{v}_a|^2 \hat{\mathbf{k}}_W$ in Zhao's Model and $\boldsymbol{l} = -\rho \boldsymbol{S}(\boldsymbol{c})\boldsymbol{v}_a$ in the Zhukovskii Glider. Again, by assuming zero sideslip, and by remembering that $\boldsymbol{c}$ lies along the wingspan of the glider, these vector are parallel by definition. The famous *Kutta-Joukowski Theorem* tells us that the magnitude of the lift can be related to the net circulation over the wing in the following manner: $|\boldsymbol{l}| = \rho |\boldsymbol{c}||\boldsymbol{v}_a|$. This means that

$$L = \frac{1}{2}\rho A c_L |\boldsymbol{v}_a|^2 = \rho |\boldsymbol{c}||\boldsymbol{v}_a| \tag{3.46}$$

must hold for Zhao's dynamics. From eq. (3.14), we already know that this is also the case for the Zhukovskii Glider. Because of this, both the magnitude and the directions of the lift vectors in the two models are equal. The gravitational forces are already equal between the models. It is therefore concluded that both models describe the motion of a point mass under the influence of the same aerodynamic forces.

3.4.2 Similarity Transformation

We now proceed to derive the similarity transformation from a state-input pair $(\boldsymbol{x}, \boldsymbol{u})$ from Zhao's dynamics to the Zhukovskii Glider, and vice versa. This will be useful for the formulation of optimization constraints later, when the trajectory optimization problem will be solved. It also serves to show how the Zhukovskii Glider in fact captures the same information as Zhao's dynamics, without the need for complex trigonometric functions.

First, given a state $(V_a, \psi, \gamma, x, y, z)$ in Zhao's dynamics, the equivalent state $(x, y, z, \dot{x}, \dot{y}, \dot{z})$ for the Zhukovskii Glider is easily found by the kinematics in eq. (3.7). The corresponding inverse transformation from a state given by the Zhukovskii Glider to the equivalent state in Zhao's dynamics is given by first calculating V_a as:

$$V_a = |\boldsymbol{v}_a| = |\boldsymbol{v} - \boldsymbol{w}| \tag{3.47}$$

where $\boldsymbol{v} = [\dot{x}, \dot{y}, \dot{z}]^\intercal$. Then, γ and ψ are calculated from an inversion of the kinematics in eq. (3.7):

$$\gamma = \arcsin\left(-\frac{\dot{z} - w_z}{V_a}\right) = \arcsin\left(-\frac{v_{a,z}}{|\boldsymbol{v_a}|}\right) \tag{3.48a}$$

$$\psi = \arccos\left(\frac{\dot{x} - w_x}{\cos\gamma}\right) \tag{3.48b}$$

Note that the singularities that arise by this inversion are exactly the same that the dynamics in eq. (3.8) suffer from, hence this transformation does not impose any additional constraints on the validity of the models.

We then proceed to seek a relation between the different input vectors $\boldsymbol{u} = [c_L, \phi]^\intercal$ and $\boldsymbol{u} = \boldsymbol{c}$. Given an input (c_L, ϕ) and a state $(V_a, \psi, \gamma, x, y, z)$ from Zhao's dynamics, the corresponding circulation vector $\boldsymbol{c}$ can be calculated. First, the magnitude is calculated by utilizing the result in eq. (3.14). Next, by remembering that $\boldsymbol{c}$ lies along the wingspan of the glider, the y-axis of the $\mathcal{W}$ frame is given as $\hat{\mathbf{j}}_W = \frac{\boldsymbol{c}}{|\boldsymbol{c}|}$, where $\hat{\mathbf{j}}_W$ is calculated from the angles ψ, γ and ϕ. Thus, given a pair $(\boldsymbol{x}, \boldsymbol{u})$ in Zhao's dynamics, the input vector in Zhukovskii Glider $\boldsymbol{u} = \boldsymbol{c}$ can be calculated as:

$$\boldsymbol{c} = \frac{1}{2} A c_L V_a \hat{\mathbf{j}}_W \tag{3.49}$$

For the inverse transformation, calculating the input $\boldsymbol{u}$ for Zhao's dynamics from a pair $(\boldsymbol{x}, \boldsymbol{u})$ given by the Zhukovskii Glider, some of the relations have already been presented. For completeness, they are briefly repeated here. The rotation matrix $\boldsymbol{R}_W^N = [\hat{\mathbf{i}}_W, \hat{\mathbf{j}}_W, \hat{\mathbf{k}}_W]$ defined in eq. (3.2) is given by $\hat{\mathbf{i}}_W = \frac{\boldsymbol{v}_a}{|\boldsymbol{v}_a|}$, $\hat{\mathbf{j}}_W = \frac{\boldsymbol{c}}{|\boldsymbol{c}|}$ and by $\hat{\mathbf{k}}_W = \hat{\mathbf{i}}_W \times \hat{\mathbf{j}}_W$. From this and from eq. (3.2), there are a number of ways to calculate the bank angle ϕ, for instance by

$$\phi = \arcsin\left(\frac{\hat{\mathbf{j}}_{W,3}}{\cos\gamma}\right) \tag{3.50}$$

where $\boldsymbol{v}_i$ denotes the i-th element of the vector $\boldsymbol{v}$, and γ is calculated from the inverse kinematics in eq. (3.48), as previously shown. Note that this expression does not

introduce any new singularities.

The lift coefficient c_L can be calculated by once again utilizing the result in eq. (3.46), which provides an expression for the lift coefficient in terms of the net circulation over the wing

$$c_L = \frac{|\boldsymbol{c}|}{\frac{1}{2}A|\boldsymbol{v}_a|} \tag{3.51}$$

As a conclusion, Zhao's dynamics and the Zhukovskii Glider are in fact mathematically equal under the two conditions that there is zero sideslip, and the lift-induced drag is given by the constant $k = \frac{1}{\mathcal{A}\pi}$, where the effective wing area A and wingspan b are given. However, the Zhukovskii Glider provides a model that is free of the singularities that comes with using Euler angles, that is, the Zhukovskii Glider is defined for $\gamma = \frac{1}{2}\pi + n\pi$, $n = 0, 1$, where Zhao's dynamics are undefined.

3.4.3 Discussion

Let us for a moment compare the relative formulation of the Zhukovskii Glider

$$\dot{\boldsymbol{v}}_a + (\frac{|\boldsymbol{v}_a|^2 + |\boldsymbol{c}|^2}{2\Lambda|\boldsymbol{v}_a|} + \boldsymbol{S}(\boldsymbol{c}) + \frac{\partial \boldsymbol{w}}{\partial \boldsymbol{p}})\boldsymbol{v}_a = \boldsymbol{e}_z \tag{3.52a}$$

$$\dot{\boldsymbol{p}} = \boldsymbol{v}_a + \boldsymbol{w} \tag{3.52b}$$

$$\boldsymbol{x} = [\boldsymbol{p}^\intercal, \boldsymbol{v}^\intercal]^\intercal, \quad \boldsymbol{u} = \boldsymbol{c} \tag{3.52c}$$

with Zhao's dynamics:

$$m\dot{V}_a = -D - mg\sin\gamma - m\dot{w}_x\cos\gamma\cos\psi \tag{3.53a}$$

$$mV_a\dot{\gamma} = -L\cos\phi - mg\cos\gamma + m\dot{w}_x \tag{3.53b}$$

$$mV_a\dot{\psi}\cos\gamma = L\sin\phi + m\dot{w}_x \tag{3.53c}$$

$$\dot{x} = V_a\cos\gamma\cos\psi + w_x \tag{3.53d}$$

$$\dot{y} = V_a\cos\gamma\sin\psi \tag{3.53e}$$

$$\dot{z} = -V_a\sin\gamma \tag{3.53f}$$

$$\boldsymbol{x} = [V, \gamma, \psi, \dot{x}, \dot{y}, \dot{z}]^\intercal, \quad \boldsymbol{u} = [c_L, \phi]^\intercal \tag{3.53g}$$

where we have assumed that the wind is zero along the y-axis and the z-axis for the latter dynamics, in order to improve readability.

By comparison, a few remarks can be made:

- For the Zhukovskii Glider, the general motion of a glider through a wind field is intuitively captured by the simple, polynomial expression. From the model, it is clear that the drag accelerates the vehicle along the negative airspeed direction, and that the circulation generates a lift that accelerates the aircraft upwards (negative z-direction). The influence of the wind field on the motion of the glider can be inferred from knowing the Jacobian. It is also clear how the drag increases quadratically with the airspeed and the circulation.

- In the Zhukovskii Glider, it is immediately clear how the physical parameters of the aircraft influences the performance. The only physical parameter that matters is the optimal glide ratio Λ, and this serves to linearly reduce or increase the drag of the glider.

- For Zhao's dynamics, it is hard or impossible to intuit from the model how the aircraft will behave.

- The state and input vector in the Zhukovskii Glider is the position and the airspeed of the glider, respectively. Important quantities for making sense of the values, like bank angle, air-relative flight path angle and lift coefficient are not immediately visible.

- In Zhao's dynamics, all of the state and input variables have a clear, physical interpretation.

In summary, the Zhukovskii Glider definitely brings with it some very positive aspects, most noticeably in terms of simplicity and readability, as it is much easier to understand how the aircraft will behave. However, physical quantities that are commonly used when talking about aircrafts are not directly visible and have to be computed from the state and input variables. The author hopes that by being

complementary to the models normally used, the Zhukovskii Glider will help bringing additional insight to the research of dynamic soaring, as well as research on fixed-wing aircrafts in general.

3.5 Parameter Values for the Glider

The values for the physical parameters that are used for the model are given in table 3.1. These values are designed to resemble those for a typical Wandering Albatross. These are the same values that have been used by multiple researchers, that was first proposed by Sachs in [3].

Parameter	Value
g $[\frac{m}{s^2}]$	9.81
m $[kg]$	8.5
A $[m^2]$	0.65
b $[m]$	3.306
$\mathcal{AR}$	16.81
$c_{D,p}$	0.033
Λ	20

Table 3.1: Values used for the glider. The values are designed to resemble those of a Wandering Albatross.

Note that the relationship between this optimal lift-to-drag ratio Λ and the other parameters satisfies the relationship in eq. (3.28) that was derived earlier.

With these parameter values, the optimal glide angle is found as $\Theta = 0.05\,\text{rad} = 2.86°$. By using eq. (3.31), this gives the optimal glide speed $V_{\text{opt}} = 12.44\text{ms}^{-1} = 44.78\text{kmh}^{-1}$.

3.6 Wind Modeling

In the context of dynamic soaring, a number of different wind models are typically used. In this section, these models will be described briefly. More importantly, they will be shown to satisfy the relationship $\frac{\partial \boldsymbol{w}}{\partial h} = g(h)\boldsymbol{w}$ where $h > 0$ implies that

$g(h) > 0$, as described in eq. (2.17), implying that the energy analysis from chapter 2 holds for all of the wind models.

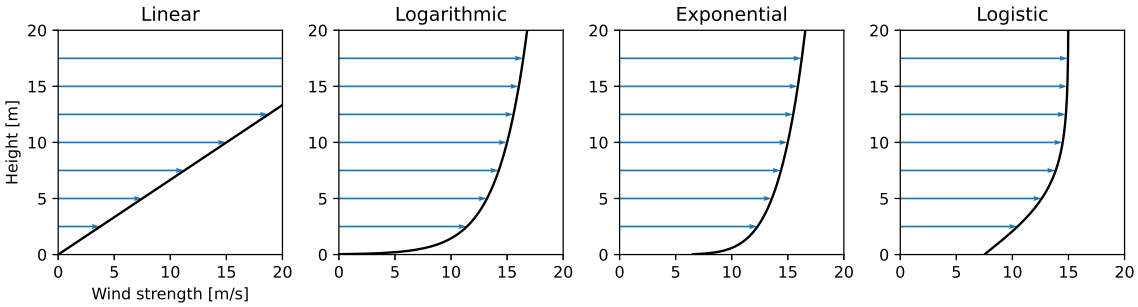

Figure 3-6: Figure showing the four different wind profiles.

All of the wind models assume that the wind is blowing along the negative North-axis, and only depends on the glider height $h(t) \triangleq -z(t)$, that is

$$\boldsymbol{w}(h) = \begin{bmatrix} -w(h) \\ 0 \\ 0 \end{bmatrix} \tag{3.54}$$

where $\boldsymbol{w}(h)$ describes the three dimensional wind-field, whereas $w(h)$ describes the wind strength at a given height. In fig. 3-6, the four different wind models are plotted.

3.6.1 Linear Model

The linear model is the simplest model of a find field. It is used in e.g. [4, 8], and is given by

$$w(h) = \frac{w_{\text{ref}}}{h_{\text{ref}}} h \tag{3.55}$$

where h_{ref} denotes some reference height, and w_{ref} denotes the wind speed at that height. The partial derivative in terms of h is given simply by $\frac{\partial w}{\partial h} = \frac{w_{\text{ref}}}{h_{\text{ref}}} = \frac{1}{h} w = g(h)w$, where $g(h) > 0$ for $h > 0$.

3.6.2 Logarithmic Model

The logarithmic model, also called the log wind profile, is commonly used to describe the vertical distribution of horizontal mean wind speeds within the lowest portion of the planetary boundary layer, typically up to about 2000 meters altitude [30]. It is used in [3] and [4].

$$w(h) = w_{\text{ref}} \frac{\ln(h/h_0)}{\ln(h_{\text{ref}}/h_0)} \tag{3.56}$$

where h_0 specifies the surface roughness length. Note that this model is only valid for altitudes $h > h_0$. The derivative is given by

$$\frac{\partial w}{\partial h} = \frac{1}{h} \frac{w_{\text{ref}}}{\ln(h_{\text{ref}}/h_0)} = \frac{1}{h \ln(h/h_0)} w = g(h)w \tag{3.57}$$

where $\ln(h/h_0) > 0$ for the validity of the model, hence $g(h) > 0$ for $h > h_0$.

This model most closely resembles the atmosphere which is where the UAV will be flying, and therefore this wind model is used throughout the thesis. A ten meter reference altitude is normal, as this is the height at which satellite based surface wind measurements are reported [31]. A surface roughness of 0.03 meters corresponds to that of a rough sea or cut grass.

3.6.3 Exponential Model

The exponential model also goes by the name of the wind profile power law, and is used in [3] and [12].

$$w(h) = w_{\text{ref}} \left(\frac{h}{h_{\text{ref}}} \right)^{\alpha} \tag{3.58}$$

where h_{ref} denotes some reference height, and w_{ref} denotes the wind speed at that height. α is a coefficient that characterizes the relative change of the wind with the height.

$$\frac{\partial w}{\partial h} = \frac{\alpha}{h} w = g(h)w \tag{3.59}$$

where $g(h) > 0$ for $h > 0$.

3.6.4 Logistic Model

The logistic model is used in [11] and [10], and describes a wind field using the Sigmoid function:

$$w(h) = \frac{w_{\text{ref}}}{1 + e^{-h/\delta}} \tag{3.60}$$

where w_0 is the free stream wind speed, and δ describes the wind shear layer thickness. The derivative reads as

$$\frac{\partial w}{\partial h} = \frac{e^{-h/\delta}}{\delta} w = g(h)w \tag{3.61}$$

where $g(h) > 0$ always.

3.6.5 Parameter Values

The values of the physical parameters that are used for this work are summarized in table 3.2.

Parameter	Value
h_{ref} $[m]$	10
w_{ref} $[m/s]$	15
h_0 $[m]$	0.03
α	0.143
$\delta[m]$	5

Table 3.2: Physical parameters used for the wind models

Chapter 4

Trajectory Optimization

The goal of dynamic soaring is to harvest energy from a wind field in order to sustain energy-neutral or energy-positive flight. This is achieved through the use of periodic motion. In order to find energy-neutral trajectories, periodic boundary conditions need to be satisfied by the trajectory. In the case of a constant wind field, this allows the trajectory to be repeated indefinitely, in theory enabling an UAV to sustain energy-neutral flight forever.

Generating periodic dynamic soaring trajectories can be accomplished by a number of different methods. Typically, dynamic soaring trajectories are generated through the use of trajectory optimization [3, 4, 7, 8, 9, 10, 12, 13, 14, 15, 22], as these methods generally are the fastest, and thus more suitable for real-time implementation. However, a multitude of different methods have been explored. Researchers have been able to obtain non-optimal soaring trajectories from explicitly integrating closed-form dynamics [19], and both genetic algorithms [17] and reinforcement learning methods [18] have been used to generate trajectories. Some attempts have even been made at generating trajectories through heuristic techniques [32], although it has later been concluded that it is easier to obtain usable results through optimal control methods [33].

A good overview and comparison of the different trajectory optimization methods used in the context of dynamic soaring is given by Bower in [4]. The speed, accuracy and robustness of the methods are compared. Three different methodologies for

trajectory optimization is tested: a collocation method, a pseudospectral method, and Fourier series in combination with differential flatness. The collocation method is the one that is proposed by Zhao in [7], where the implementation of the method is based on third order Gauss-Lobatto quadrature. Pseudospectral methods are similar to collocation methods, except that higher order, global polynomials are typically used, together with intelligently chosen control points. The pseudospectral method is the Gauss pseudospectral method and the Radu pseudospectral method, implemented with the optimal control software GPOPS. The last method based on differential flatness is implemented from the work by Deittert et al. in [12]. Here, the system is shown to be differentially flat in the flat output space (x, y, z) and their derivatives, in the case where the glider is supplied with a propeller that is generating thrust. A Fourier series representation of the trajectories is used to enforce the periodic boundary conditions. All optimization problems are solved with the solver *Sparse Nonlinear Optimization*, more widely known as SNOPT [34].

The method that was found by Bower to be the most efficient and robust was the collocation method first proposed by Zhao in [7]. By implementing the method with analytic gradients, Bower achieved a solve time of approximately two seconds. The collocation method is the same as the one used by Slotine et al. in [11] and [10]. In fact, this is also the same collocation method that was first proposed for general trajectory optimization by Hargraves and Paris in [35] back in 1987, and further generalized for Gauss-Lobatto quadratures by Herman et al. in [36]. This method is now commonly referred to as *Direct Collocation*. Because this is a method that is found to work well by a number of other authors, and by comparison with other approaches in [4] came out as the fastest and most robust method, it is also used in this work.

4.1 Direct Collocation

To obtain an accurate solution with a limited number of function evaluations, a collocation method is well suited. Collocation methods enforce that the dynamics of the

system are satisfied at a set of collocation points, and use a set of piecewise polynomials to describe the trajectory. By only enforcing the dynamics at the collocation points, it does not actually require discrete dynamics, unlike many other trajectory optimization methods. Thus, the continuous dynamics can in fact be directly implemented, and any problems with numerical instability because of discretization through numerical integration are eliminated. The implementation for Direct Collocation used in this thesis follows the problem formulation as specified in the original paper by Hargraves and Paris [35], which is compactly summarized by Tedrake in [37]. This work follows the notation of the latter.

In *Direct Collocation*, the state trajectory $\boldsymbol{x}(t)$ is described as a piecewise cubic spline, and the input trajectory $\boldsymbol{u}(t)$ as a piecewise first-order hold. The points between the polynomial segments are called break points, and the midpoints of the polynomial segments are chosen as collocation points. As will be shown, this particular combination makes it possible to simply implement the values of the polynomials and their slopes at the break points as decision variables, in contrast to using the polynomial coefficients as decision variables. An illustration of this can be seen in fig. 4-1. This makes it simpler to impose additional constraints on the trajectory, and this is also the combination of polynomials and degrees that was found to work best for general trajectory optimization in [35].

We start by defining the dynamical system as

$$\dot{\boldsymbol{x}} = \boldsymbol{f}(\boldsymbol{x}, \boldsymbol{u}) \tag{4.1}$$

We want to enforce the dynamics only at the collocation points. In order to formulate these constraints, we first seek to define the values of the trajectory at the collocation points by the values and the slopes of the trajectory at the break points.

First, we start with the state trajectory $\boldsymbol{x}(t)$. For each polynomial segment k, defined for $[t_k, t_{k+1}]$, let $s(t) = \frac{t-t_k}{T}$ where $\Delta t_k = t_{k+1} - t_k$ is the length of the segment, such that $s \in [0, 1]$. This lets us define each polynomial segment as a polynomial defined only for $s \in [0, 1]$. Then a state trajectory for a single state i for

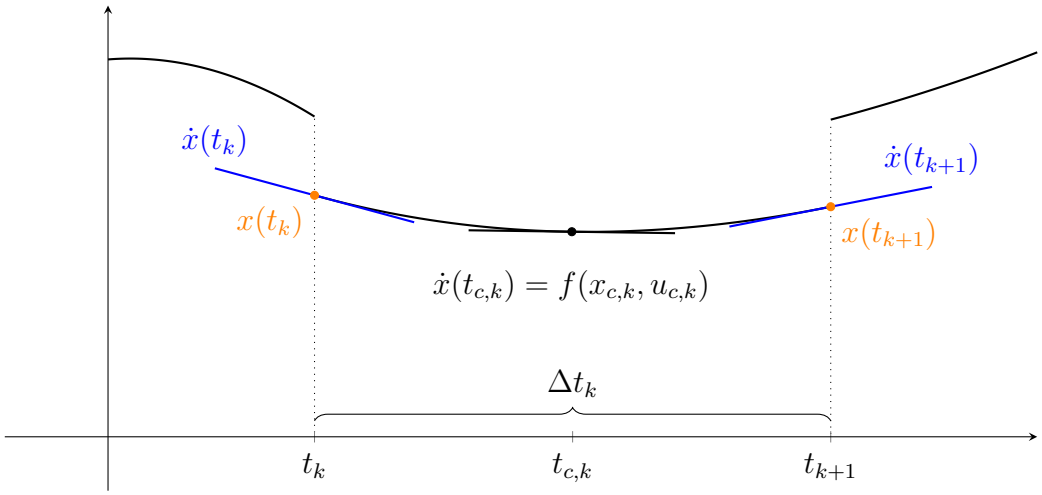

Figure 4-1: Illustration of the decision variables at the break points t_k and t_{k+1} for one piecewise polynomial used in Direct Collocation. The dynamics are only enforced at the collocation point $t_{c,k}$, and are satisfied by modifying the values and slopes at the break points.

.

that segment can be defined as

$$x_i(s) = c_{i,0} + c_{i,1}s + c_{i,2}s^2 + c_{i,3}s^3 \tag{4.2}$$

Differentiation of $\boldsymbol{x} = \boldsymbol{x}(s(t))$ along $s = s(t)$ for a given segment k gives

$$\dot{\boldsymbol{x}} = \frac{d\boldsymbol{x}}{dt} = \frac{\partial \boldsymbol{x}}{\partial s}\frac{ds}{dt} = \frac{\partial \boldsymbol{x}}{\partial s}\frac{1}{\Delta t} \implies \frac{\partial \boldsymbol{x}}{\partial s} = \Delta t \dot{\boldsymbol{x}} \tag{4.3}$$

Evaluate $x_i(s)$ at the break points $x_i(t_k) = x_i(s=0)$ and $x_i(t_{k+1}) = x_i(s=1)$, and then let $\dot{x}_i(t_k) = \frac{1}{\Delta t}\frac{\partial x}{\partial s}\Big|_{s=0}$ and $\dot{x}_i(t_{k+1}) = \frac{1}{\Delta t}\frac{\partial x}{\partial s}\Big|_{s=1}$ be the slopes evaluated at the break points. By differentiation of eq. (4.2) and by evaluating the result at the break points $s = 0$ and $s = 1$, one obtains the following relation

$$\begin{bmatrix} 1 & 0 & 0 & 0 \\ 0 & 1 & 0 & 0 \\ 1 & 1 & 1 & 1 \\ 0 & 1 & 2 & 3 \end{bmatrix} \begin{bmatrix} c_{i,0} \\ c_{i,2} \\ c_{i,2} \\ c_{i,3} \end{bmatrix} = \begin{bmatrix} x_i(t_k) \\ \Delta t \dot{x}_i(t_k) \\ x_i(t_{k+1}) \\ \Delta t \dot{x}_i(t_{k+1}) \end{bmatrix} \tag{4.4}$$

which, by inverting the matrix, gives

$$\begin{bmatrix} c_{i,0} \\ c_{i,2} \\ c_{i,2} \\ c_{i,3} \end{bmatrix} = \begin{bmatrix} 1 & 0 & 0 & 0 \\ 0 & 1 & 0 & 0 \\ -3 & -2 & 3 & -1 \\ 2 & 1 & -2 & 1 \end{bmatrix} \begin{bmatrix} x_i(t_k) \\ \Delta t \dot{x}_i(t_k) \\ x_i(t_{k+1}) \\ \Delta t \dot{x}_i(t_{k+1}) \end{bmatrix} \tag{4.5}$$

Now, by evaluating the trajectory given by eq. (4.2) at the collocation points at $s = \frac{1}{2}$, and by applying the results from eq. (4.3) and eq. (4.5), one obtains the interpolated value of x at the collocation point $t_{c,k} \triangleq \frac{1}{2}(t_k + t_{k+1})$

$$\boldsymbol{x}(t_{c,k}) = \frac{1}{2}(\boldsymbol{x}(t_k) + \boldsymbol{x}(t_{k+1})) + \frac{\Delta t}{8}(\dot{\boldsymbol{x}}(t_k) - \dot{\boldsymbol{x}}(t_{k+1})) \tag{4.6}$$

In the same way, the slope at the collocation point can be found as

$$\dot{\boldsymbol{x}}(t_{c,k}) = -\frac{3}{2\Delta t}(\boldsymbol{x}(t_k) - \boldsymbol{x}(t_{k+1})) - \frac{1}{4}(\dot{\boldsymbol{x}}(t_k) + \dot{\boldsymbol{x}}(t_{k+1})) \tag{4.7}$$

The goal of the trajectory optimization is to find a trajectory where the difference between this slope and the actual dynamics defined in eq. (4.1) are driven to zero.

For the input trajectory, it is simpler to define the value of $\boldsymbol{u}$ at the collocation point $t_{c,k}$ in terms of $\boldsymbol{u}(t_k)$ and $\boldsymbol{u}(t_{k+1})$. Since $\boldsymbol{u}$ is defined as a first order hold, it is simply

$$\boldsymbol{u}(t_{c,k}) = \frac{1}{2}(\boldsymbol{u}(t_k) + \boldsymbol{u}(t_{k+1})) \tag{4.8}$$

We can now formulate the following, nonlinear trajectory optimization problem:

$$\begin{aligned} \min_{\boldsymbol{x}(\cdot),\boldsymbol{u}(\cdot),\Delta t} \quad & J = l_F(\boldsymbol{x}[N]) + \sum_{n=0}^{N-1} l(\boldsymbol{x}[n], \boldsymbol{u}[n]) \\ \text{subject to} \quad & \dot{\boldsymbol{x}}(t_{c,n}) = \boldsymbol{f}(\boldsymbol{x}(t_{c,n}), \boldsymbol{u}(t_{c,n})) \quad \forall n \in [0, N-1] \\ & \boldsymbol{x}[0] = \boldsymbol{x}_0 \\ & \boldsymbol{lb} \leq \boldsymbol{c}(\boldsymbol{x}[k], \boldsymbol{u}[k]) \leq \boldsymbol{ub} \end{aligned} \tag{4.9}$$

where the decision variables to the problem are the state and input evaluated at the N break points, $\boldsymbol{x}[k] = \boldsymbol{x}(t_k)$ and $\boldsymbol{u}[k] = \boldsymbol{u}(t_k)$, as well as the segment length Δt. $\dot{\boldsymbol{x}}(t_{c,k})$ is defined in eq. (4.7). $l(\boldsymbol{x}[k], \boldsymbol{u}[k])$ is any desired cost function of the state and input, and $l_F(\boldsymbol{x}[N])$ is the cost for the final state. Any additional, linear or nonlinear constraints on the input or on the states can easily be added to the problem at the desired breakpoints k, as indicated by the last inequality constraint $\boldsymbol{c}(\boldsymbol{x}[k], \boldsymbol{u}[k])$. Equality constraints are implemented as inequality constraints where the lower and upper bounds are set equal.

Note that the length Δt_k of the time segments could in theory be set as a individual decision variable without requiring further complexity. However, for the purposes of this thesis, the segment lengths are chosen to be equal, and are implemented as a single variable.

4.2 Numerical Solution to Dynamic Soaring

The goal of the trajectory optimization is to find a periodic trajectory that maximizes the average ground speed of the glider towards the desired heading ψ, given the parameters describing the glider and the wind field. That is, to find a trajectory that satisfies both the dynamics of the glider, additional constraints imposed by the glider on the state and input trajectories, and to satisfy periodic boundary conditions on the state and input.

The entire optimization problem will be formulated as stated in eq. (4.9). Note that since the optimization problem is formulated with the equal segment lengths $\Delta t_k = h$ as a decision variables, the optimization problem will implicitly search for the period of the trajectory, by letting the trajectory shrink and grow through time. The end time $t_f = Nh$ is retrieved from the solution, and from this the period of the solution is calculated as $T_{period} = \frac{1}{t_f}$ and the average horizontal velocity as $\boldsymbol{v}_{avg} = \frac{d}{T}$, where d is the total horizontal distance travelled, defined in eq. (4.12).

The relative formulation of the Zhukovskii Glider as presented in section 3.3.1, eq. (3.44), with the state $\boldsymbol{x} = [\boldsymbol{p}^\intercal, \boldsymbol{v}_a^\intercal]^\intercal$, is used as the dynamical model. In order to

improve the numerical properties of the problem, the variables are first re-scaled as shown in section 3.3.4 before formulating the optimization problem, and then scaled back after solving the optimization problem. The dynamics given by eq. (3.44) are thus required to be satisfied by the trajectory by implementing equality constraints at the collocation points as shown in eq. (4.9). Let $\boldsymbol{x}[k] \triangleq \boldsymbol{x}(t_k)$, and define $h \triangleq -z$ as the height of the glider. The initial position is chosen as $\boldsymbol{p}_0 = [0, 0, h_0]$, whereas the initial velocity is free.

4.2.1 Constraints and Cost Function

Periodicity Constraints

In order to travel in the desired direction given by the heading ψ, a relative constraint on the final x and y coordinates can be given by trigonometry, assuming that the glider always starts in the origin. The periodic boundary constraints are implemented as follows

$$\boldsymbol{v}[0] = \boldsymbol{v}[N] \tag{4.10a}$$

$$h[0] = h[N] \tag{4.10b}$$

$$x[N] = y[N] \tan \psi \tag{4.10c}$$

where the last constraint is replaced by

$$x[0] = x[N] \quad \text{if} \quad \psi = 0 \quad \text{, or} \tag{4.10d}$$

$$y[0] = y[N] \quad \text{if} \quad \psi = \frac{1}{2}\pi + n\pi, \quad n = 0, 1 \tag{4.10e}$$

It is desired that the trajectory be periodic in both the height, the velocities and the circulation of the glider. This is implemented as the following, simple equality

constraints:

$$h[0] = h[N] \tag{4.11a}$$

$$\boldsymbol{v}_a[0] = \boldsymbol{v}_a[N] \tag{4.11b}$$

$$\boldsymbol{c}[0] = \boldsymbol{c}[N] \tag{4.11c}$$

Note that since the height is forced to be equal at the first and the last point, the wind speeds will also be equal at these points. Hence, periodicity on the inertial velocity $\boldsymbol{v}$ are actually implemented as equality constraints on the relative airspeed $\boldsymbol{v}_a$, as seen above.

Travel Distance and Average Velocity

To avoid loitering trajectories that start and end in the same coordinates, a constraint is added to enforce that the total distance, defined as d, covered along the desired direction is always positive

$$d_{\min} \leq d[N] \triangleq \begin{bmatrix} \sin\psi \\ \cos\psi \end{bmatrix}^{\mathsf{T}} \begin{bmatrix} x[N] \\ y[N] \end{bmatrix} \tag{4.12}$$

The goal of the optimization is to maximize the average velocity in the desired direction. This is achieved by adding the following nonlinear term to the cost function

$$l_F \triangleq -Q\frac{d[N]}{N\Delta t} \tag{4.13}$$

where Q is a linear weight.

Input Rates

To ensure that the generated trajectories are realistic, high input rates are penalized. The input is a piecewise linear trajectory, and the input rates are found through a

first order, forward, finite difference matrix in the following manner:

$$\dot{\boldsymbol{u}}(\cdot) \triangleq \begin{bmatrix} \dot{u}[0] \\ \dot{u}[1] \\ \vdots \\ \dot{u}[N-1] \end{bmatrix} = \frac{1}{\Delta t} \begin{bmatrix} -1 & 1 & 0 & \cdots & 0 \\ 0 & -1 & 1 & \cdots & 0 \\ \vdots & & & \ddots & 1 \\ 0 & \cdots & & & -1 \end{bmatrix} \begin{bmatrix} u[0] \\ u[1] \\ \vdots \\ u[N-1] \end{bmatrix} \tag{4.14}$$

The input rates are constrained to be small by adding the following nonlinear (remember that Δt is a decision variable) term to the cost function:

$$l \triangleq R\dot{\boldsymbol{u}}(\cdot)^{\intercal}\dot{\boldsymbol{u}}(\cdot) \tag{4.15}$$

where R is a linear weight. The total cost function now reads as

$$J = l_F + l = -Q\frac{d[N]}{N\Delta t} + R\dot{\boldsymbol{u}}(\cdot)^{\intercal}\dot{\boldsymbol{u}}(\cdot) \tag{4.16}$$

Physical Constraints

The height is constrained by linear inequality constraints:

$$h_{\min} \leq h[k] \leq h_{\max} \quad \forall\, k = 0, 1, \ldots, N \tag{4.17}$$

In order to generate a realistic input for the glider, the circulation has to be constrained. To achieve a physical interpretation of the circulation values, the constraint on the circulation is added by constraining the corresponding lift coefficient. From eq. (3.51) one has that

$$c_l = \frac{|\boldsymbol{c}|}{\frac{1}{2}a|\boldsymbol{v}_a|} \implies c_l^2 = \frac{1}{\frac{1}{4}a}\frac{\boldsymbol{c}^{\intercal}\boldsymbol{c}}{\boldsymbol{v}_a^{\intercal}\boldsymbol{v}_a} \tag{4.18}$$

which makes it possible to constrain the lift coefficient through the following inequality constraint

$$0 \leq c_{\mathrm{l,min}}^2 \leq \frac{1}{\frac{1}{4}a}\frac{\boldsymbol{c}[k]^{\intercal}\boldsymbol{c}[k]}{\boldsymbol{v}_a[k]^{\intercal}\boldsymbol{v}_a[k]} \leq c_{\mathrm{l,max}}^2 \quad \forall\, k = 0, 1, \ldots, N-1 \tag{4.19}$$

where the constraint has been squared to improve the numerical properties of the optimization problem. Note that this constraint stays the same whether the variables are fully dimensionalized or dimensionless as defined in eq. (3.40), as the characteristic values cancels out.

The bank angle is also constrained. A reformulation of eq. (3.50) gives

$$\sin\phi = \frac{\hat{\mathbf{j}}_{W,3}}{\cos\gamma} \implies \sin^2\phi = \frac{c_3^2}{\boldsymbol{c}^\intercal\boldsymbol{c}\left(1-\frac{v_{a,3}^2}{\boldsymbol{v_a}^\intercal\boldsymbol{v_a}}\right)} \tag{4.20}$$

where the fact that $\hat{\mathbf{j}}_{W,3} = \frac{c_3}{|\boldsymbol{c}|}$ and $\sin\gamma = -\frac{v_{a,3}}{|\boldsymbol{v}_a|} \implies \cos\gamma = \sqrt{1-\frac{v_{a,3}^2}{\boldsymbol{v_a}^\intercal\boldsymbol{v_a}}}$ has been used. Note that also here, the constraint is squared to improve the numerical properties of the optimization problem. The constraint is implemented as

$$\frac{c_3[k]^2}{\boldsymbol{c}[k]^\intercal\boldsymbol{c}[k]\left(1-\frac{v_{a,3}[k]^2}{\boldsymbol{v_a}[k]^\intercal\boldsymbol{v_a}[k]}\right)} \leq \sin^2\phi_{\max} \quad \forall\, k = 0,1,\ldots,N-1 \tag{4.21}$$

Another property that is crucial for getting realistic trajectories is the load factor. The load factor n is defined as the total lift divided by the weight of the vehicle:

$$n = \frac{|\boldsymbol{l}|}{mg} = \frac{\rho|\boldsymbol{c}||\boldsymbol{v}_a|}{mg} \tag{4.22}$$

which, when using the dimensionless variables defined in eq. (3.40), reduces to the very simple expression

$$n = |\bar{\boldsymbol{v}}_a||\bar{\boldsymbol{c}}| \tag{4.23}$$

The load factor required for the trajectory is thus constrained as

$$|\bar{\boldsymbol{v}}_a[k]||\bar{\boldsymbol{c}}[k]| \leq n_{\max} \quad \forall\, k = 0,1,\ldots,N-1 \tag{4.24}$$

4.2.2 Constraint Values

The physical values of the different optimization parameters used throughout the initial condition, constraints and cost function is given in the following table:

Parameter	Value
h_0	5 $[m]$
$h_{\min}$	0.5 $[m]$
$h_{\max}$	100 $[m]$
$d_{\min}$	0.67 L $[m]$
$c_{\mathrm{l,min}}$	0
$c_{\mathrm{l,max}}$	1.5
$\phi_{\max}$	80°
$n_{\max}$	3

Table 4.1: Values for the constraints of the trajectories.

where L denotes the characteristic length of the glider, as defined in eq. (3.40). The weights for the cost function are given as

Parameter	Value
Q	1
R	0.01

Table 4.2: Weights for the cost function in the optimization problem.

4.3 Solving the Optimization Problem

4.3.1 Optimization Software

The optimization problem is formulated in the framework Drake [38] using Python 3.8. For the optimization problem, SNOPT [34] is chosen as the solver. For calculation of derivatives, Drake employs the automatic differentiation module of Eigen3 [39], which implements forward differentiation through the use of a computational graph and the chain rule. Both Drake and Eigen3 are implemented in C++.

SNOPT is a general-purpose solver for constrained optimization, that minimizes a linear or nonlinear function subject to bounds on the variables and sparse linear or nonlinear constraints. The problem of generated dynamic soaring trajectories through direct collocation is a nonlinear program with sparse constraints, as most constraints only depends on the knot points at the given time t_k, or at most at t_k and t_{k+1} at the same time. Therefore, a sparse, nonlinear solver such as SNOPT is well suited.

In order to find locally optimal solutions, SNOPT uses a Sequential Quadratic Programming (SQP) algorithm. The further details of this solver are beyond the scope of this work. Interested readers are referred to the documentation found at [34].

The full implementation of the work in this thesis can be found at [16].

4.3.2 Initial Guess

In this work, a simple linear initial guess based on the performance parameters of the glider was found to work well. When generating a single trajectory, the solver is given a linear trajectory as an initial guess for the state. For the input, it is given a zero trajectory, where some Gaussian white noise with zero mean and a very low variance is added, in order to make it easier for the solver to find a solution. When incrementally generating multiple trajectories, the solution for the previous, neighbouring trajectory is used as an initial guess. In most cases, this allowed solve times of 1-2 seconds. A similar approach is used in [12], whereas a sinusoidal initial guess is used in [4, 7].

The linear, initial guess used for the optimization problem is based on the optimal glide speed at level flight V_l of the glider, as defined in section 3.3.1. First, an average velocity guess is calculated from the performance parameter of the glider as $V_{\text{avg}} = 2V_l$, together with a guess for the period of the trajectories. The final position is then calculated as $\boldsymbol{p}(t_f) = [V_{\text{avg}} T \sin\psi,\, V_{\text{avg}} T \cos\psi,\, h_0]^\intercal$, and the initial guess for the position trajectory is calculated as a linear interpolation between x_0 and x_f. The velocity guess is set accordingly as the constant vector $\boldsymbol{v} = [V_{\text{avg}} \sin\psi,\, V_{\text{avg}} \cos\psi,\, 0]^\intercal$. The period guess is chosen as $T = 7$.

Chapter 5

Numerical Results

For the first few experiments, individual trajectories generated by the trajectory optimizer will be examined. Three types of trajectories will be examined: upwind, crosswind, and downwind trajectories. The trajectories will be shown to be periodic and energy-neutral, allowing them to be repeated indefinitely. An energy analysis will be performed on each trajectory from the perspective of the analysis in chapter 2, and the inputs will be shown to conform to the constraints given in section 4.2.2. Characteristics for each trajectory will also be examined, including the resulting period, average velocity and the total distance covered.

For the last experiment, trajectories are generated for all directories $\psi \in [0°, 360°]$, and presented as a polar plot. The maximum average horizontal velocities, along with the corresponding periods, will be presented. A sample gallery of the different trajectories along the polar will be shown.

For the generation of trajectories in this work, solution times ranged from between a second to a minute, depending on the initial guess and the desired travel angle. $N = 31$ was chosen as the number of collocation points, similar to [7].

5.1 Going Upwind

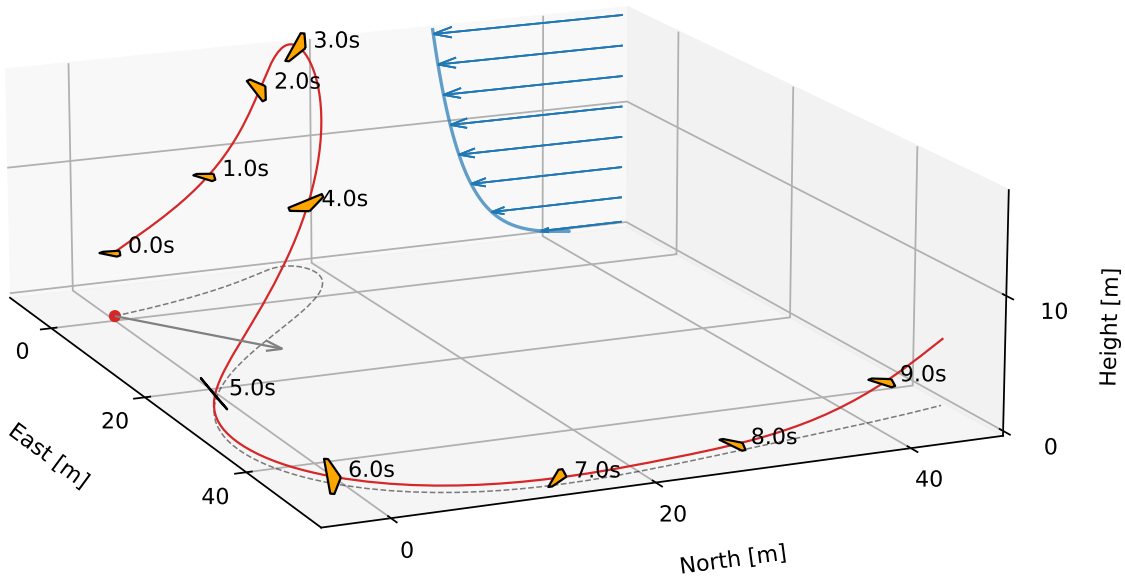

Figure 5-1: Dynamic soaring trajectory at 45° towards the wind.

As our first experiment, the trajectory optimization is tasked with finding a trajectory at $\psi = 45°$ against the wind. The resulting trajectory can be seen in figs. 5-1 and 5-2. The total horizontal distance covered along the desired travel trajectory is 65.6m over a period of 9.2s, giving an average horizontal velocity of 7.16ms^{-1}. From the trajectory, it immediately seems that the glider behaves as the energy analysis from chapter 2 predicted; the glider first rises against the wind, then completes a 180° turn before diving with the wind. It continues flying against the wind at a very low altitude, before rising into the wind and performing another turn. The maneuver is periodic, both in terms of altitude, velocities and the input.

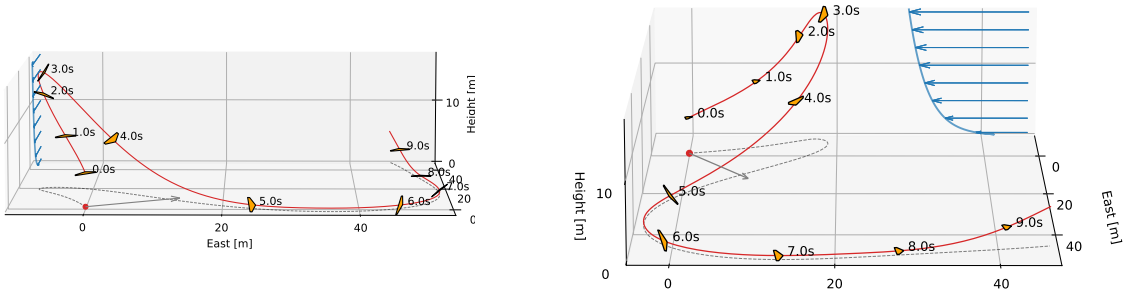

Figure 5-2: A detailed look at the trajectory.

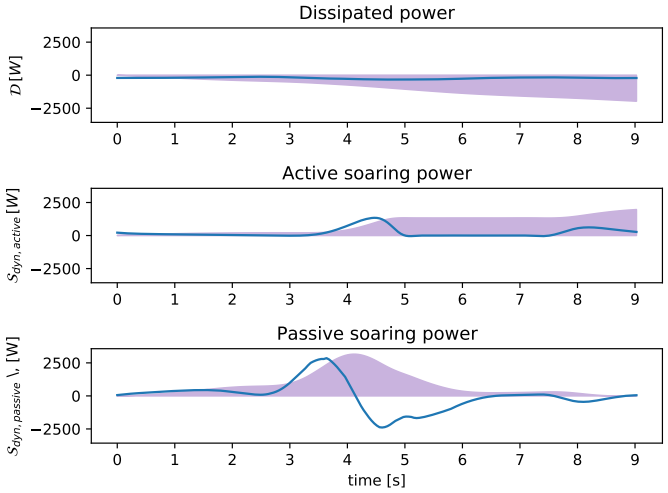

Figure 5-3: The mechanism of energy harvesting shown during a soaring trajectory. The powers are plotted with blue lines, and the energy is plotted in purple as the integral of the power. The active soaring power is non-zero and positive only when the glider is diving with the wind, or rising against it.

A plot of the dissipated power $\mathcal{D}$, the active soaring power $\mathcal{S}_{\text{dyn,active}}$, and the passive soaring power $\mathcal{S}_{\text{dyn,passive}}$, as defined in chapter 2, can be found in fig. 5-3. From this plot, a few conclusions can be drawn. First, the dissipated energy is always negative, and only contributes to reduce the total energy in the system. Second, the integral of the passive soaring power is zero over a cycle, showing that this term does not contribute to the net energy over a cycle. Finally, when looking at the soaring power over the course of a cycle, it is only positive twice: Once at $t = 4$s when the vehicle is diving with the wind, and once at $t = 8$s when the vehicle starts rising against the wind. This behaviour is expected, as it is consistent with the energy

analysis performed in chapter 2. Nevertheless, remember that the energy analysis is performed on a general point-mass, while the trajectories are generated from a complex model of a glider. This shows how the seemingly simple energy analysis captures the essential principles of complex, soaring flight.

As the trajectory is energy-neutral and not energy-positive, this means that the energy gained from the active soaring power $\mathcal{S}_{\text{dyn,active}}$ must equal the energy lost from the dissipative power $\mathcal{D}$. This is reflected in the numerical experiment, and the phenomenon can be seen in fig. 5-6.

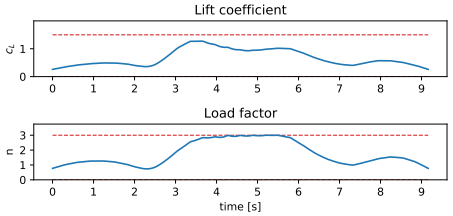

(a) The lift coefficient and the load factor calculated from the trajectory.

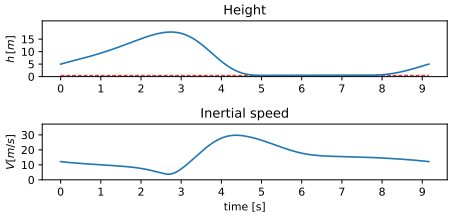

(b) The height and inertial speed. The height is at its minimum value for most of the flight.

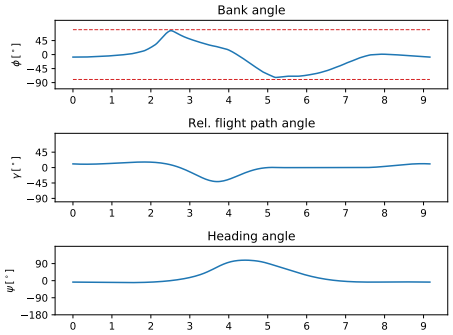

(c) The angles of the aircraft during flight.

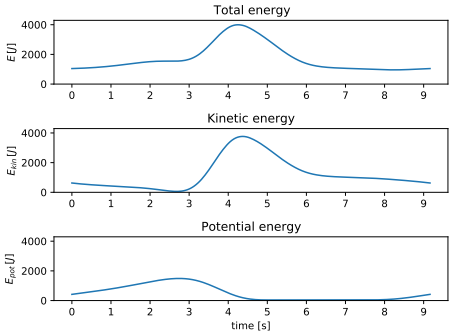

(d) The energy of the system during a soaring trajectory. Over a cycle, the trajectory is energy-neutral.

Figure 5-4: Physical quantities required by the trajectory. All values are plotted with blue lines. Constraints are shown with red, dashed lines.

The height h and the inertial airspeed of the glider $|\boldsymbol{v}|$ are plotted in fig. 5-4b, and the overall energy in the system E, E_{kin} and E_{pot} are plotted in fig. 5-4d. By looking at the energy plot, it is clear that the trajectory is energy-neutral over a cycle. The lift coefficient c_L, and load factor n are plotted in fig. 5-4a. The resulting bank angle ϕ, the air-relative heading γ, and the heading angle ψ are plotted in fig. 5-4c.

Note that these values have to be computed from the resulting trajectory, as they are not direct products of the optimization. The computation is performed by using the results in section 4.2.1. From these plots, it is clear that all constraints on physical values are satisfied. In fact, it is only the load factor and the height that reaches their constraints. The load factor is at its maximum once the aircraft starts banking after diving in the direction of the wind. The height is always at its minimum when the vehicle is not performing the turn.

5.2 Going Crosswind

Next, a crosswind trajectory at $\psi = 90°$ is generated. In this case, the trajectory is found to be strongly sinusoidal. The trajectory can be seen in fig. 5-5. The average horizontal velocity is 24.7ms^{-1}, with a period of 4.5s, covering a total horizontal distance of 111m.

Once again, the trajectory is seen to adhere to the principles of energy harvesting. As expected, the aircraft rises against the wind, and descends with the wind. From the energy analysis in fig. 5-6, this can be seen even clearer: at both $t = 2$s and at $t = 4$s, the vehicle gains energy trough the active soaring power $\mathcal{S}_{\text{dyn,active}}$. $t = 2$s is precisely when the vehicle is descending with the wind, and $t = 4$s is when it starts rising against the wind. The total energy gained from the active soaring power is equal to the energy lost from the dissipation power.

The important physical quantities of the trajectory can be seen in fig. 5-7. In contrast to when travelling at $\psi = 45°$, both the bank angle and the load factor are now closer to their limits. The load factor is at its maximum permitted value for the entire duration of the low turn where the glider turns into the wind. The bank angle comes close to its maximum limit during both turns. Also for this case, the glider stays at the minimum height when it is not performing the turn.

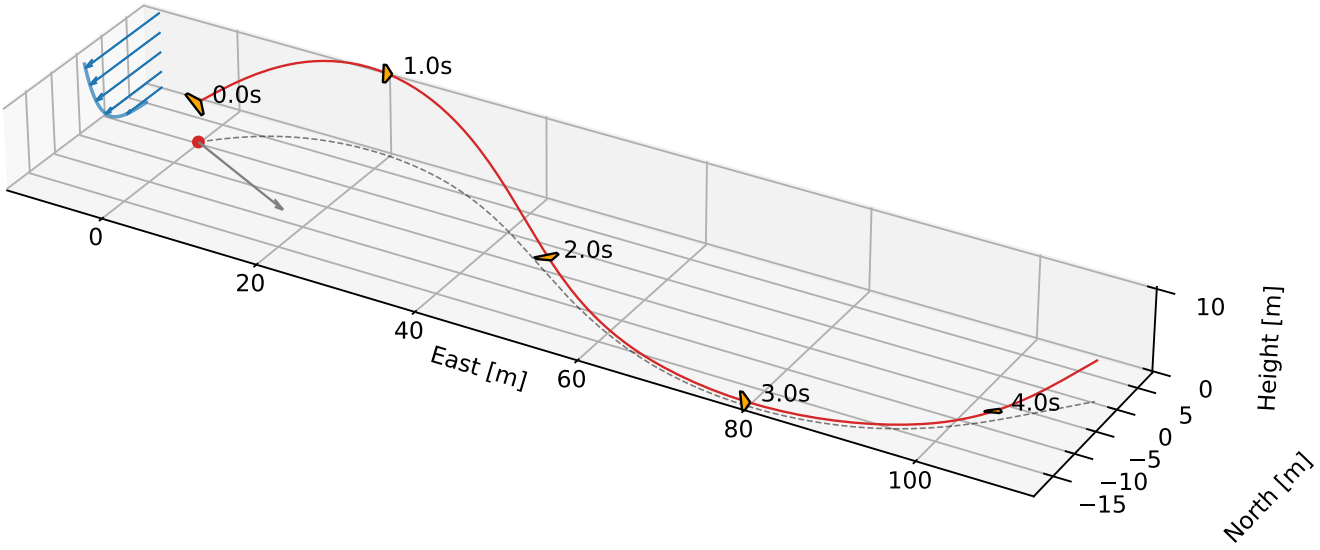

Figure 5-5: Trajectory for travelling perpendicular to the wind. The trajectory resembles a sine curve.

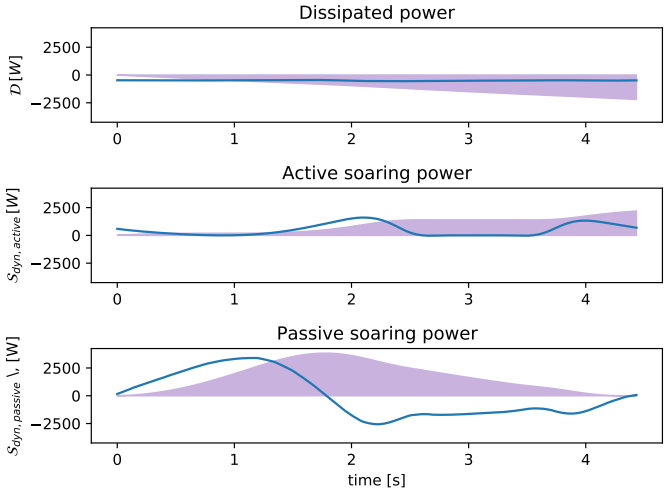

Figure 5-6: Energy mechanism for the crosswind trajectory.

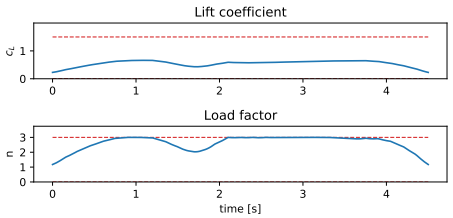

(a) The lift coefficient and the load factor calculated from the trajectory.

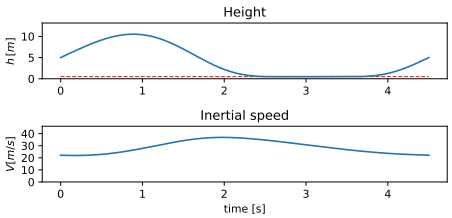

(b) The height and inertial speed.

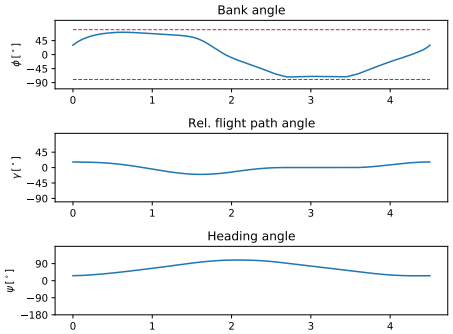

(c) The angles of the aircraft during flight.

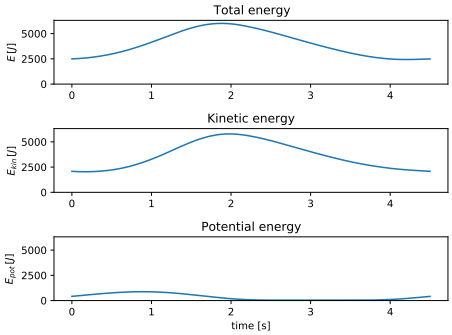

(d) The energy of the system during a soaring trajectory.

Figure 5-7: Important physical quantities for the crosswind trajectory.

5.3 Travelling Downwind

Next, a downwind trajectory is generated at $\psi = 135.5°$, the angle at which the vehicle reaches its overall maximum horizontal velocity. For this angle, the vehicle reaches a velocity of $33.2\text{m}\,\text{s}^{-1}$, at a period of 5.6s, covering a total distance of 185.9m. The trajectory can be seen in fig. 5-8.

Here, the glider only gains significant energy at one point during the trajectory. From $t = 2$s to $t = 4$s, the glider dives with the wind, and from the plot, it can be seen that it is during this time that energy is harvested.

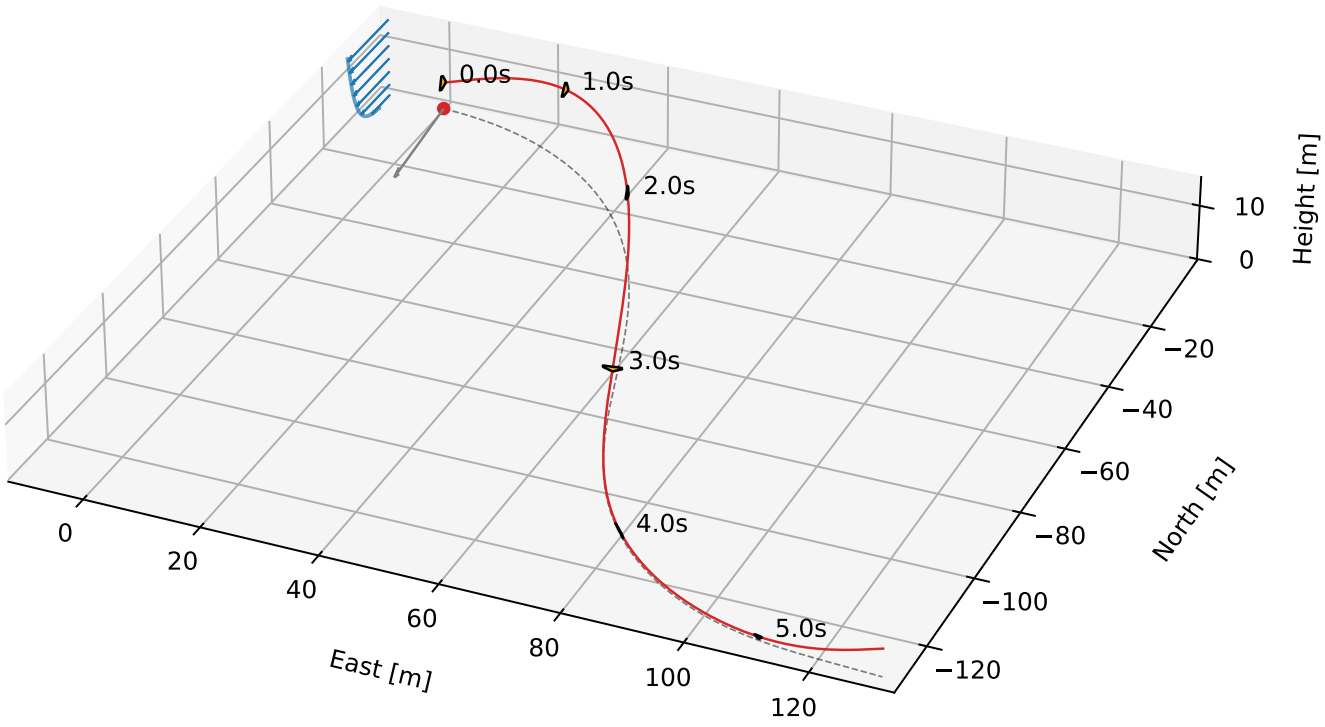

Figure 5-8: The downwind trajectory at which the glider reaches its maximum velocity.

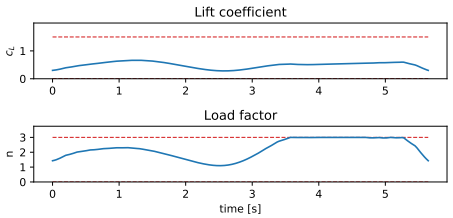

(a) The lift coefficient and the load factor calculated from the trajectory.

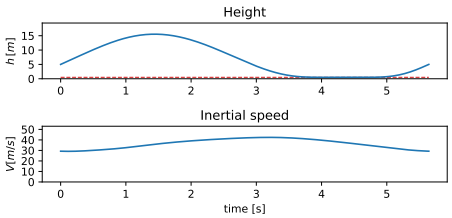

(b) The height and inertial speed.

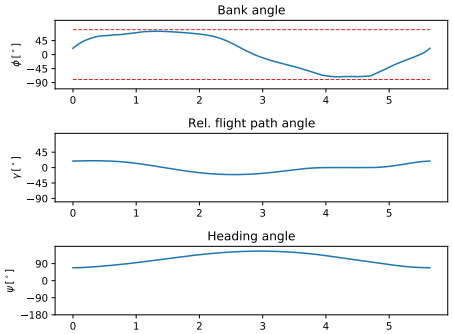

(c) The angles of the aircraft during flight.

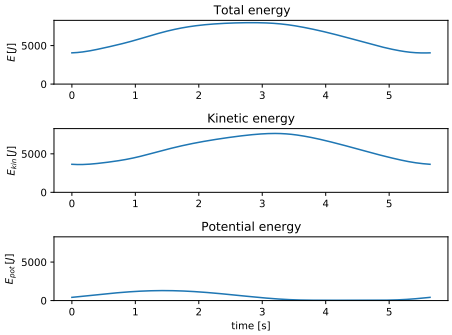

(d) The energy of the system during a soaring trajectory.

Figure 5-9: Important physical quantities for the downwind trajectory.

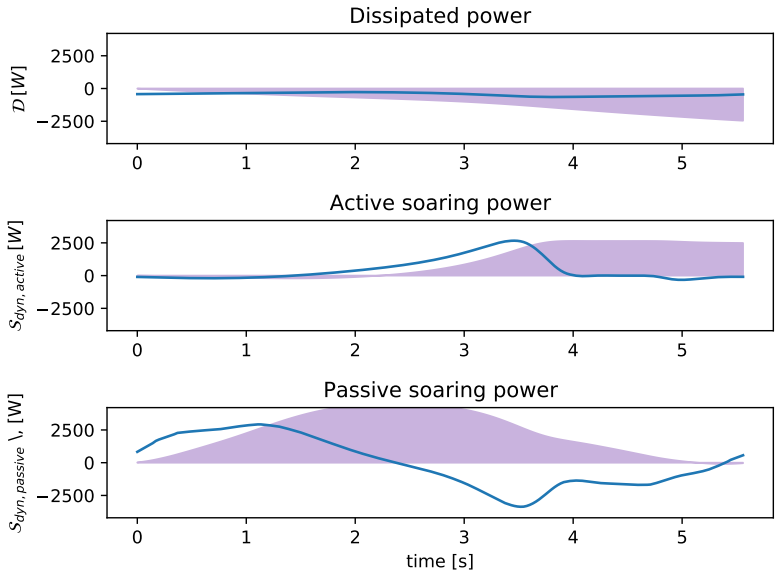

Figure 5-10: Energy mechanism for the downwind trajectory

5.4 Maximum Achievable Speeds in All Directions

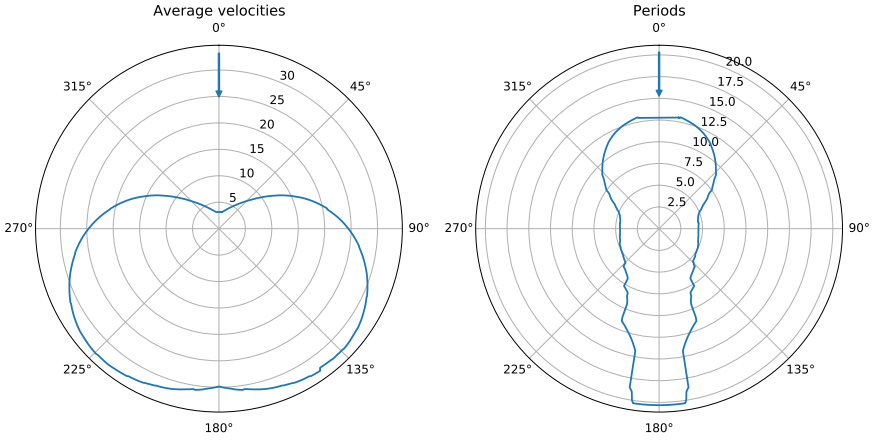

Figure 5-11: A polar plot showing the maximum reachable average horizontal velocities for every travel angle ψ, together with the corresponding periods.

Finally, for the last experiment, trajectories are generated for all angles to the wind $\psi \in [0°, 360°]$. The first trajectory is found with a straight line as an initial guess, then the travel angle is incremented by 0.5° for every step, while the previous solution is used as the initial condition for the solver. The result can be seen in fig. 5-11. A gallery of the trajectories at different travel angles can be seen in fig. 5-12, and an animation showing all the trajectories can be found at [16].

Average velocities range from $3\mathrm{m\,s^{-1}}$ to $33\mathrm{m\,s^{-1}}$, with periods between 5s to 21s. It is desirable to compare this with findings from nature. In [11], it is reported that Wandering Albatrosses travelling in *crosswind* directions has a typical dynamic soaring maneuver that lasts for 5-15 seconds, and extends over 50-150 meters. If considering crosswind as being from 90° to somewhere less than 180°, this is very consistent with the findings from the polar plot in fig. 5-11.

The plot also indicates that the maximum velocity is not reached when travelling directly with the wind. In fact, the maximum velocity is reached at an angle of $\psi = 224.5°$ and $\psi = 135.5°$, at a speed of $33.19\mathrm{ms^{-1}} = 119.5\mathrm{kmh^{-1}}$. Comparing this to the optimal level glide speed $V_l = 12.4\mathrm{ms^{-1}}$, the maximum achieved horizontal velocity is more than doubled. In general, the glider is able to fly relatively fast for

both crosswind and downwind trajectories. When going upwind, the velocity is much lower, and reaches speeds as low as $3\text{ms}^{-1} = 10.8\text{kmh}^{-1}$.

From the plot, it is clear that both the average horizontal velocities and the corresponding periods are very much symmetric. This makes intuitive sense, as it should not matter which side of the wind the glider is flying at. However, some numerical inaccuracies can still be seen in the plots, as is to be expected when working with numerical optimization.

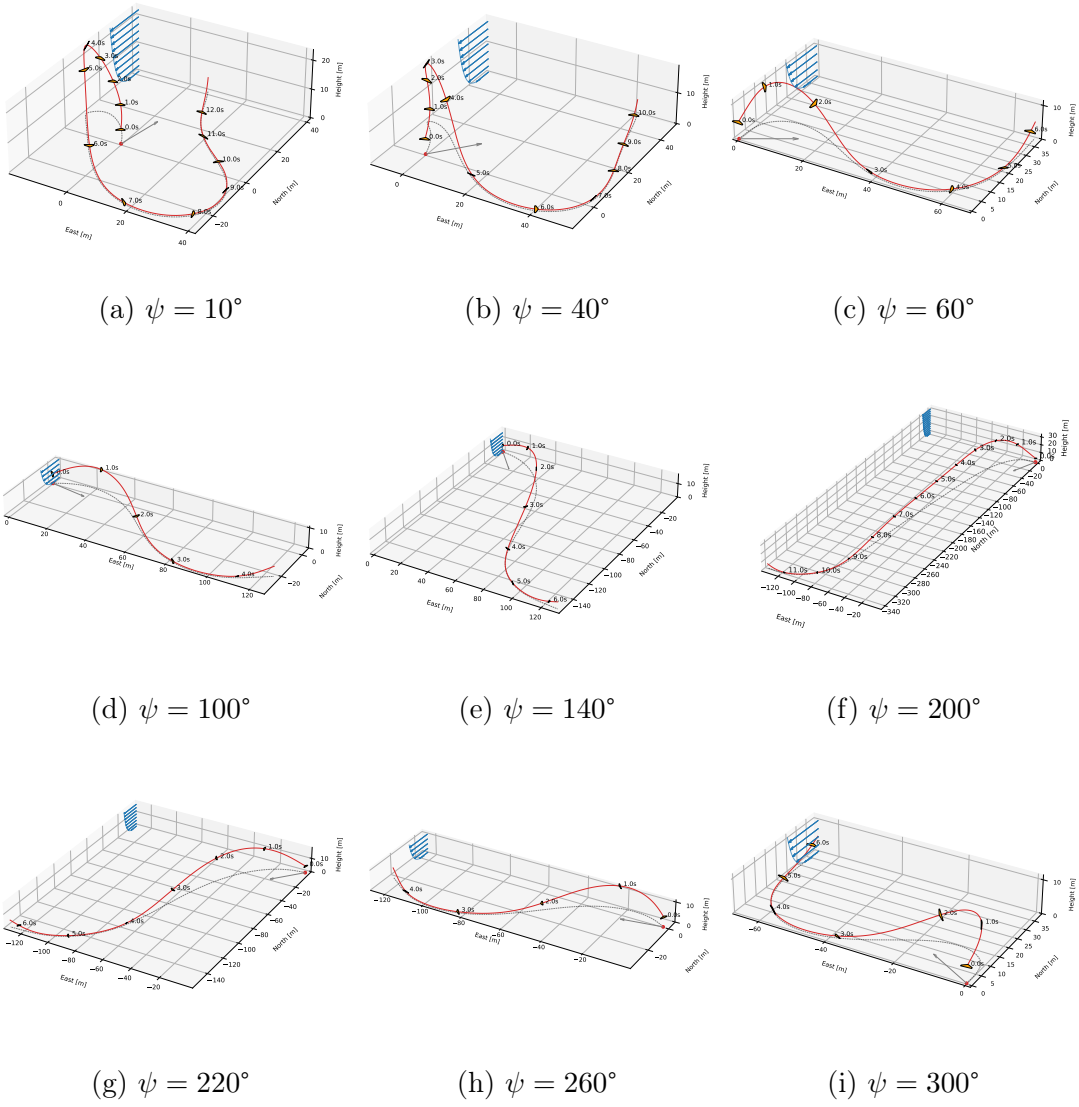

(a) $\psi = 10°$ (b) $\psi = 40°$ (c) $\psi = 60°$

(d) $\psi = 100°$ (e) $\psi = 140°$ (f) $\psi = 200°$

(g) $\psi = 220°$ (h) $\psi = 260°$ (i) $\psi = 300°$

Figure 5-12: A gallery of sample trajectories in different directions to the wind.

Chapter 6

Future Work and Conclusions

6.1 Future Work

This work proposes a new look at the energy mechanisms during soaring flight, together with a new way of modeling flight through a wind field. The thesis also presents a framework for the generation of trajectories in any given direction, as well as an overview of the achievable speeds. There are some quite interesting directions in which this work can be taken.

6.1.1 High-level Trajectory Planning

As stated in the conclusion, the most efficient way to reach a goal is not necessarily to travel directly towards it; for dynamic soaring, it is actually more efficient to combine travel at different angles where one reaches higher speeds. This technique is called *tacking*, and is commonly used by sailboats when travelling cross-wind. A planner that incorporates this concept for dynamic soaring should be proposed and tested.

At an even higher level, a planner that creates a plan for most efficiently travelling across different wind-fields would be required to allow an unpowered UAV to cover long distances. Given information about the achievable travel speeds in the different directions for each wind field, this resembles a weighted shortest path problem. It could be solved with optimization, where algorithms such as Dijkstra or A* could

provide a good initial guess to the optimization problem. In [4] such a high-level planner based on isochrones is proposed.

6.1.2 Trajectory Stabilization

When it comes to implementing dynamic soaring on a real aircraft, the generated trajectories must be stabilized by an onboard controller. There are some well-known control methods for stabilizing trajectories, such as the nonlinear control method Sliding Mode Control as described by Slotine and Li in [40]. Optimal control such as Time-Varying LQR control or Receding Horizon MPC control are also good candidates for trajectory stabilization. Both [19] and [4] list multiple works dealing with trajectory stabilization for fixed-wing aircrafts.

However, one interesting aspect of dynamic soaring is that the trajectory need not be stabilized in time. That is, the trajectory is periodic, and under the assumption that the wind field is independent of time, it does not matter when the aircraft reaches the different parts of the trajectory. Therefore, trajectory stabilization for *periodic* trajectories are most suited for this task. One idea is to let the phase-shift of the trajectory be a control variable, essentially allowing the controller to move the trajectory back and forth in time to best stabilize the trajectory. Another very interesting idea is to use an infinite horizon MPC controller for periodic tasks, such as the one proposed by Todorov et al. in [41].

6.1.3 Transition Between Trajectories

Another question is how the aircraft should transition into a trajectory and between trajectories. In this work, the aircraft is required to start at a given initial height, but the initial velocities, bank angle and lift coefficient can be chosen arbitrarily (within the physical constraints). However, in real life, the aircraft needs to get to this initial position somehow. Given a high-level planner that supplies the glider with new travel angles every now and then in order to most efficiently reach a goal destination, the aircraft must also be capable of transitioning between trajectories.

This is a problem that could potentially be solved by a trajectory stabilizing controller, but it could also be solved as a trajectory optimization problem on its own. The formulation would sound as follows: Given a wind field, an initial state and an end state (the starting state for the next dynamic soaring trajectory), design a trajectory that gets the glider from the initial state to the end state without the use of a thrust-generating propeller.

6.1.4 Online Trajectory Update

This work constitutes a framework for offline trajectory generation, which could potentially be deployed for online generation from one trajectory to the next. However, this framework is too slow to update the current trajectory in an online manner. Given changes in the wind field, it is desirable to be able to do so. In [21] Hong et al. propose an approach for doing real-time modifications to a pre-computed trajectory in order to improve it for new wind measurements. They formulate a convex QP problem based on the deviations from the nominal trajectory, which can be solved online. Further investigation into how a trajectory generation scheme, such as the one presented in this thesis, integrates with an online modification method such as the one presented by Hong in [21] should be explored.

6.2 Conclusions

This thesis focused on the offline generation of trajectories for dynamic soaring. A novel 3-DOF point mass model was used for the generation of trajectories, and a new energy analysis of soaring flight was proposed. Trajectories for travel at different angles to the wind have been generated and analysed in perspective of the new energy analysis framework. The author hope that this work will serve as a foundation for future exploration of dynamic soaring, and that we one day will see a self powered UAV circumnavigating the globe without the use of propulsive power.

From the work in this thesis, a few conclusions can be drawn:

- The energy harvesting process of dynamic soaring maneuvers is no longer ambiguous. Without going into details of modelling or aerodynamics, the analysis in chapter 2 clearly states how any point-mass travelling through a three dimensional wind field is able to harvest energy: by descending with the wind, or by rising against the wind. The result is proven mathematically, and is supported by the results from chapter 5.

- A new, polynomial model of a point mass travelling through a wind field has been proposed and verified through numerical experiments. By giving a more intuitive description of the motion of a point-mass travelling through a wind field, this new model is complementary to the conventional 3-DOF point mass model based on trigonometry and Euler angles that is typically used by other researchers.

- A 3-DOF point mass model seems to be able to generate realistic trajectories, as the distances, velocities and periods are consistent with what is typically reported for the Wandering Albatross. Velocities, structural loads on the aircraft, the ability to generate lift and the required angles and rates are all within reasonable values. It seems that neglecting the rotational dynamics of the aircraft is a justified assumption, as the trajectories that are generated are very realistic and consistent with what is observed in nature.

- By using dynamic soaring, the aircraft is able to fly at a speed of more than double of the optimal level glide speed of the glider. The maximum average horizontal velocity is reached at an angle of $\psi = 135.5°$ and $\psi = 224.5°$. At this angle to the wind, the aircraft reaches a velocity of almost double of the optimum level glide speed.

- The vehicle seems to stay at the minimum height for as long as possible during the trajectory. It only increases the height when it has to perform a turn to sustain the flight.

- For a wind field of sufficient (and physically reasonable) strength, the aircraft is

able to travel in all directions. However, the most efficient way to travel is not necessarily to travel directly in the desired direction, as the average horizontal velocities are low when travelling directly upwind.

In summary, this work focused on the trajectories required for dynamic soaring. The world has yet to see a real bio-inspired robotics Albatross flying across the Atlantic without the use of propulsive energy, and there are several challenges that needs to be tackled before this can be achieved. The author hopes that the results presented in this work can contribute to the field of research within dynamic soaring.

Bibliography

[1] J.P. Croxall et al. "Global circumnavigations: tracking year-round ranges of nonbreeding albatrosses". In: *Science* (2005).

[2] L Rayleigh. "The Soaring of Birds". In: *Nature* 27 (1883), pp. 534–535. DOI: 10.1038/027534a0.

[3] G. Sachs. "Minimum shear wind strength required for dynamic soaring of albatrosses". In: *Ibis* 147 (2004), pp. 1–10.

[4] Geoffrey Bower. "Boundary Layer Dynamic Soaring for Autonomous Aircraft: Design and Validation". PhD thesis. Dec. 2011. DOI: 10.13140/RG.2.1.5081.0085.

[5] Chinmay K. Patel, Hak-Tae Lee, and I. Kroo. "Extracting Energy from Atmospheric Turbulence". In: *Technical Soaring* (2008).

[6] *New World Record Speed of 545mph with the Transonic DP at Bird Spring Pass!* http://www.dskinetic.com/. 2018.

[7] Y. Zhao. "Optimal patterns of glider dynamic soaring". In: *Optimal Control Applications and Methods* 25 (2004), pp. 67–89.

[8] Y. Zhao and Y. Qi. "Minimum fuel powered dynamic soaring of unmanned aerial vehicles utilizing wind gradients". In: *Optimal Control Applications and Methods* 25 (2004), pp. 211–233.

[9] N Akhtar, J F Whidborne, and A K Cooke. "Real-time optimal techniques for unmanned air vehicles fuel saving". In: *Proceedings of the Institution of Mechanical Engineers, Part G: Journal of Aerospace Engineering* 226.10 (2012), pp. 1315–1328.

[10] Gabriel Bousquet, Michael Triantafyllou, and Jean-Jacques Slotine. "Asymptotic Solution to the Rayleigh Problem of Dynamic Soaring". In: *arXiv* (Sept. 2015).

[11] G. Bousquet, M. Triantafyllou, and J. Slotine. "Optimal dynamic soaring consists of successive shallow arcs". In: *Journal of The Royal Society Interface* 14 (2017).

[12] Markus Deittert et al. "Engineless unmanned aerial vehicle propulsion by dynamic soaring". In: *Journal of Guidance Control and Dynamics* 32 (2009), pp. 1446–1457.

[13] Imran Mir, Sameh Eisa, and Adnan Maqsood. "Review of Dynamic Soaring: Technical Aspects, Nonlinear Modeling Perspectives and Future Directions". In: *Nonlinear Dynamics* 94 (Dec. 2018). DOI: 10.1007/s11071-018-4540-3.

[14] Gottfried Sachs et al. "Flying at No Mechanical Energy Cost: Disclosing the Secret of Wandering Albatrosses". In: *PloS one* 7 (Sept. 2012), e41449. DOI: 10.1371/journal.pone.0041449.

[15] Purnanand Elango and R. Mohan. "Trajectory optimisation of six degree of freedom aircraft using differential flatness". In: *Aeronautical Journal* 122 (2018), pp. 1788–1810.

[16] Bernhard Paus Græsdal. *Dynamic Soaring for Fixed-Wing UAVs*. Implementation is available online at: https://github.com/bernhardpg/dynamic-soaring. 2020.

[17] M. Boslough. "Autonomous Dynamic Soaring Platform for Distributed Mobile Sensor Arrays". In: *University of North Texas Libraries, UNT Digital Library, https://digital.library.unt.edu* (2002).

[18] C. Montella and J. R. Spletzer. "Reinforcement learning for autonomous dynamic soaring in shear winds". In: *2014 IEEE/RSJ International Conference on Intelligent Robots and Systems*. 2014, pp. 3423–3428. DOI: 10.1109/IROS.2014.6943039.

[19] Jean-Marie Kai, T. Hamel, and Claude Samson. "Novel Approach to Dynamic Soaring Modeling and Simulation". In: *Journal of Guidance, Control, and Dynamics* 42 (Mar. 2019), pp. 1–11. DOI: 10.2514/1.G003866.

[20] John Bird et al. "Closing the Loop in Dynamic Soaring". In: *AIAA Guidance, Navigation, and Control Conference* (Jan. 2014).

[21] Haichao Hong et al. "Dynamic Soaring in Unspecified Wind Shear: A Real-time Quadratic-programming Approach". In: *2019 27th Mediterranean Conference on Control and Automation (MED)* (2019), pp. 600–605.

[22] G. Sachs and P. Bussotti. "Application of optimal control theory to dynamic soaring of seabirds". In: *Variational Analysis and Applications* 25 (2005), pp. 975–994.

[23] O. Yakimenko. "Direct Method for Rapid Prototyping of Near-Optimal Aircraft Trajectories". In: *Journal of Guidance Control and Dynamics* 23 (2000), pp. 865–875.

[24] Joseph Katz and Allen Plotkin. *Low-Speed Aerodynamics*. 2nd ed. Cambridge Aerospace Series. Cambridge University Press, 2001. DOI: 10.1017/CBO9780511810329.

[25] Morten Dinhoff Pedersen. "Thoughts on Dynamic Soaring". Technical note. 2020.

[26] John Valasek. "Small Unmanned Aircraft: Theory and Practice Randal W. Beard and Timothy W. McLain". In: *Journal of Guidance, Control, and Dynamics* 36 (Jan. 2013), pp. 344–345. DOI: 10.2514/1.61067.

[27] M. Jackson, Y. Zhao, and R. Slattery. "Sensitivity of Trajectory Prediction in Air Traffic Management". In: *Journal of Guidance Control and Dynamics* 22 (1999), pp. 219–228.

[28] W. Phillips and Deryl Snyder. "Modern Adaptation of Prandtl's Classic Lifting-Line Theory". In: *Journal of Aircraft - J AIRCRAFT* 37 (July 2000), pp. 662–670. DOI: 10.2514/2.2649.

[29] Thor Fossen. *Handbook of Marine Craft Hydrodynamics and Motion Control*. May 2011. ISBN: 978-1119991496. DOI: 10.1002/9781119994138.

[30] K. J. Weston. "Boundary layer climates (Second edition). By T. R. Oke. Methuen. 1987. Pp. 435 + xvi." In: *Quarterly Journal of the Royal Meteorological Society* 114.484 (1988), pp. 1568–1568.

[31] T. Oke and Canada. "Initial guidance to obtain representative meteorological observations at urban sites". In: *World Meteorological Organization: Instruments and Observing Methods* (Jan. 2006).

[32] T. Kiceniuk. "Dynamic Soaring and Sailplane Energetics". In: *Technical Soaring* 25 (2001), pp. 221–227.

[33] J. Wharington. "Heuristic control of dynamic soaring". In: *2004 5th Asian Control Conference (IEEE Cat. No.04EX904)* 2 (2004), 714–722 Vol.2.

[34] Philip Gill et al. "SNOPT: An SQP algorithm for large-scale constrained optimization". In: *SIAM Review* 47 (Apr. 2001). DOI: 10.1137/S0036144504446096.

[35] C. Hargraves and Stephen Paris. "Direct Trajectory Optimization Using Nonlinear Programming and Collocation". In: *AIAA J. Guidance* 10 (July 1987), pp. 338–342. DOI: 10.2514/3.20223.

[36] A. L. Herman and B. Conway. "Direct optimization using collocation based on high-order Gauss-Lobatto quadrature rules". In: *Journal of Guidance Control and Dynamics* 19 (1996), pp. 592–599.

[37] Russ Tedrake. *Underactuated Robotics: Algorithms for Walking, Running, Swimming, Flying, and Manipulation (Course Notes for MIT 6.832)*. 2020. URL: http://underactuated.mit.edu/ (visited on 10/15/2020).

[38] Russ Tedrake and the Drake Development Team. *Drake: Model-based design and verification for robotics*. https://drake.mit.edu. 2019.

[39] Gaël Guennebaud, Benoît Jacob, et al. *Eigen v3*. http://eigen.tuxfamily.org. 2010.

[40] J. Slotine and W. Li. In: *Applied Nonlinear Control*. 1991.

[41] T. Erez, Y. Tassa, and E. Todorov. "Infinite-Horizon Model Predictive Control for Periodic Tasks with Contacts". In: *Robotics: Science and Systems*. 2011.